iScience

CellPress
OPEN ACCESS

Article

Altering heparan sulfate suppresses cell abnormalities and neuron loss in *Drosophila presenilin* model of Alzheimer Disease

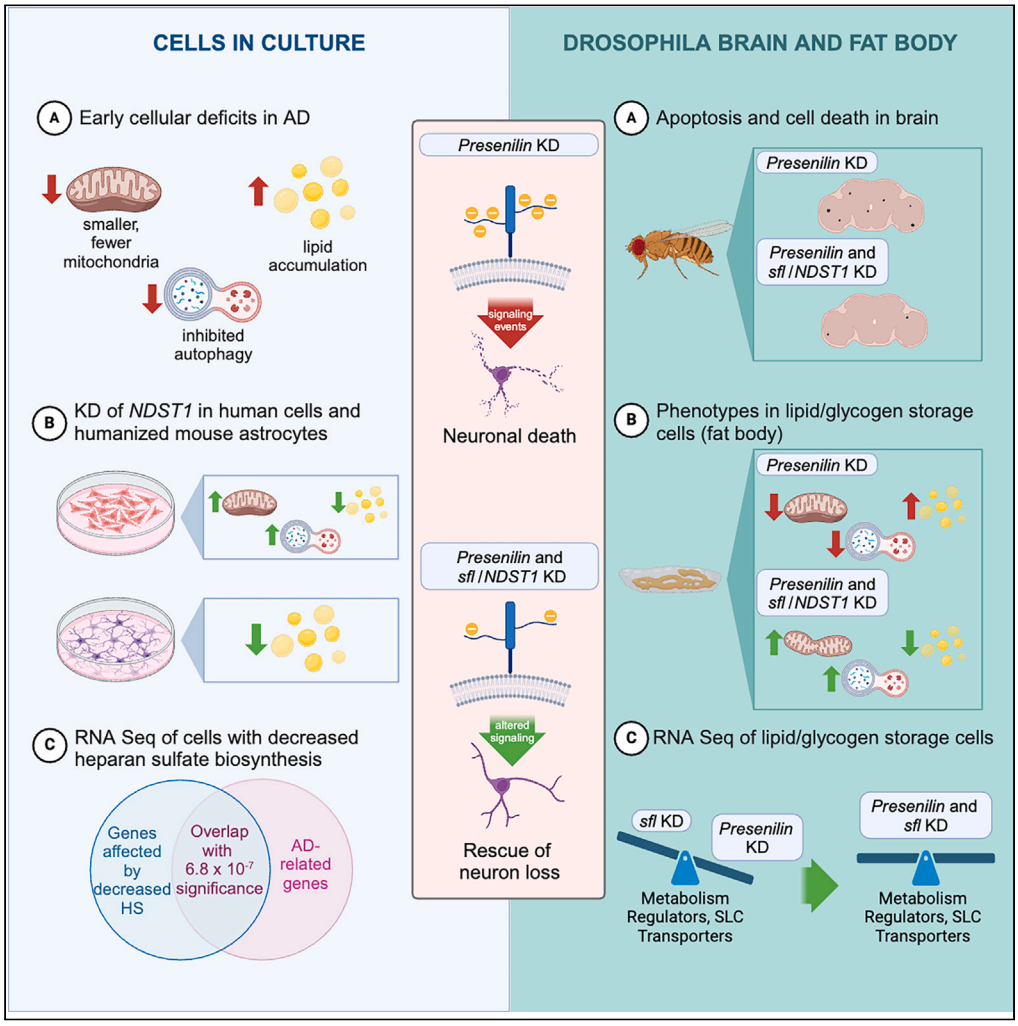

Nicholas Schultheis, Alyssa Connell, Alexander Kapral, ..., Tripti Saini, Ryan J. Weiss, Scott B. Selleck

sbs24@psu.edu

Highlights

Heparan sulfate (HS) affects autophagy, mitochondria, and lipid metabolism

AD-related gene transcripts overrepresented in HS-dependent transcriptome

Reducing HS sulfation rescues neuronal loss in *presenilin*-deficient *Drosophila*

Cell deficits mediated by *presenilin* knockdown suppressed by reduced HS sulfation

Schultheis et al., iScience 27, 110256
July 19, 2024
https://doi.org/10.1016/j.isci.2024.110256

iScience

CellPress
OPEN ACCESS

Article

Altering heparan sulfate suppresses cell abnormalities and neuron loss in *Drosophila presenilin* model of Alzheimer Disease

Nicholas Schultheis,[1] Alyssa Connell,[1] Alexander Kapral,[1] Robert J. Becker,[1] Richard Mueller,[1] Shalini Shah,[1] Mackenzie O'Donnell,[1] Matthew Roseman,[1] Lindsey Swanson,[1] Sophia DeGuara,[1] Weihua Wang,[2] Fei Yin,[2] Tripti Saini,[3] Ryan J. Weiss,[3] and Scott B. Selleck[1,4,*]

SUMMARY

We examined the function of heparan-sulfate-modified proteoglycans (HSPGs) in pathways affecting Alzheimer disease (AD)-related cell pathology in human cell lines and mouse astrocytes. Mechanisms of HSPG influences on *presenilin*-dependent cell loss were evaluated in *Drosophila* using knockdown of the *presenilin* homolog, *Psn*, together with partial loss-of-function of *sulfateless (sfl)*, a gene specifically affecting HS sulfation. HSPG modulation of autophagy, mitochondrial function, and lipid metabolism were shown to be conserved in human cell lines, *Drosophila*, and mouse astrocytes. RNA interference (RNAi) of *Ndst1* reduced intracellular lipid levels in wild-type mouse astrocytes or those expressing humanized variants of *APOE*, *APOE3*, and *APOE4*. Neuron-directed knockdown of *Psn* in *Drosophila* produced apoptosis and cell loss in the brain, phenotypes suppressed by reductions in *sfl* expression. Abnormalities in mitochondria, liposomes, and autophagosome-derived structures in animals with *Psn* knockdown were also rescued by reduction of *sfl*. These findings support the direct involvement of HSPGs in AD pathogenesis.

INTRODUCTION

More than 100 years ago, Alois Alzheimer described a dementia condition associated with a triad of histopathological abnormalities: extracellular deposits of amyloid, intracellular aggregations or neurofibrillary tangles, and accumulation of intracellular lipid in glia, described as "adipose saccules."[1] These pathological features have guided the strategies to develop a pharmaceutical for Alzheimer disease (AD), and amyloid peptide generation and deposition (neuritic plaques) has been one of the principal targets of these efforts. Recently, two antibody pharmaceuticals that reduce the levels of amyloid peptides have been approved by Food and Drug Administration (FDA), and one shows demonstrable slowing of cognitive loss.[2,3] A third antibody pharmaceutical directed against Aβ, donanemab, has shown effectiveness in slowing disease progression in a recent clinical trial.[4] Despite these successes, there is good reason to identify cellular and molecular pathologies that occur early in the AD process. Further investment in broad, mechanistic approaches to AD development is required to effectively prevent and treat this disease at a level that significantly alters the disease trajectory.

Considerable evidence from a variety of experimental approaches has shown that there are cellular deficits common to AD, implicated in both early, familial AD where causative genetic changes have been identified, as well as late-onset AD, where GWAS studies have found many risk-associated variants that influence AD susceptibility.[5–7] Pathway analyses show enrichment for genes involved in cholesterol metabolism, amyloid plaque and neurofibrillary tangle formation, membrane trafficking, and the innate immune system.[5] Many of the cellular and molecular processes embedded within these gene sets are mechanistically connected.[8] Autophagy, a vital membrane trafficking process compromised in AD, not only removes protein aggregates and damaged organelles (such as mitochondria via mitophagy) but is required for the catabolism of lipids via lipophagy. Mitochondria are also a critical nexus in these mechanisms, providing the catabolic machinery to break down fatty acids via β-oxidation and providing ATP to support cell energetics in the process.

The cellular and molecular events that accompany AD are represented in experimental models of the disease. Many of these are based on human genetic data where specific gene deficits produce early onset, severe AD and allow detailed examination of the cellular and molecular changes that initiate cell demise.[9] *PSEN1* mutations are the most common cause of familial AD, show dominant inheritance, and produce a cognitive decline in the fourth decade with greater than 90% penetrance.[10] The vast majority (90%) of clinically identified *PSEN1* mutations are loss or reduction in function alleles, reducing the activity of the γ-secretase, suggesting that the dominant inheritance results from reductions

[1]Department of Biochemistry and Molecular Biology, Pennsylvania State University, University Park, PA 16802, USA
[2]Center for Innovation in Brain Science and Department of Pharmacology, University of Arizona, Tucson, AZ 85721, USA
[3]Department of Biochemistry and Molecular Biology, Complex Carbohydrate Research Center, University of Georgia, Athens, GA 30602, USA
[4]Lead contact
*Correspondence: sbs24@psu.edu
https://doi.org/10.1016/j.isci.2024.110256

in the activity of this critical protein and its associated complex.[11] Recently, the intersection of early and late-onset AD genetics was further highlighted by the discovery of a rare *APOE* variant, *ApoE3 Christchurch (APOE3ch)*, that was associated with the protection of cognitive decline in a 70-year-old with a disease-causing *PSEN1* mutation.[12] Homozygosity for *APOE3ch* in this individual was also associated with reduced accumulation of Tau, whereas amyloid deposition was unabated and significantly higher than in younger cohorts with cognitive symptoms but lacking the *APOE3ch* variant. The amino acid change in *ApoE3ch* provided a clue as to the mechanism of this variant providing protection against AD symptoms. APOECh bears a change in a lysine residue within the heparan-sulfate-binding domain of the protein. Biochemical studies with purified APOE proteins demonstrated that APOECh showed dramatically reduced affinity for heparin, a highly sulfated form of heparan sulfate. Furthermore, APOE4, APOE3, and APOE2 proteins showed heparin affinities correlated with their relative risk for developing late-onset AD, with higher affinities associated with greater risk. Finally, a recent report showed that mice expressing a humanized *ApoE3ch* variant showed altered microglial responses and suppression of Aβ-induced Tau seeding and spread.[13] These results suggest that heparan-sulfate-modified proteins participate in APOE functions that can modulate AD pathogenesis and influence *PSEN1*-mediated events.

Heparan-sulfate-modified proteins or proteoglycans (HSPGs) are abundant molecules of the cell surface and extracellular matrix. The glycan modifications have an important role in their function, serving as binding sites for a wide array of proteins, including growth factors and growth factor receptors. HSPGs modulate the activity of many signaling events, generally serving to increase the activity of secreted protein growth factors. HSPGs are an important class of coreceptors at the cell surface, promoting the assembly of signaling complexes. HSPGs are known to affect signaling via PI3kinase, Akt, and mitogen-activated protein kinase (MAPK) systems.[14,15] HSPGs regulate Wnt, Hh, fibroblast growth factor (FGF), and bone morphogenetic protein (BMP) signaling during development and play a role in both endocytosis and exocytosis of a variety of molecules.[16–19]

We have previously shown that reducing heparan sulfate chain length or sulfation increases autophagy flux in muscle and fat body cells in *Drosophila*.[20] Modest reductions in two critical HS biosynthetic enzyme-encoding genes, *sulfateless (sfl)* and *tout velu (ttv)*, either by mutation or RNAi, also rescue cell degeneration in a model of AD mediated by expression of a dominant-negative form of presenilin in the retina.[21] Cell death and mitochondrial dysmorphology in *parkin* mutants, a model for Parkinson, are also suppressed by reducing HS function, and rescue depends on an intact autophagy system.[21] Autophagy flux and mitochondrial function, both governed by HSPG activity, are compromised by *PSEN1* deficits.[22–25] In this study, we examine in detail the effects of HSPGs on autophagy, mitochondrial function, and intracellular lipid droplets or liposomes in human cells and mouse astrocytes. Transcriptome changes in human cells defective for HS synthesis reflect the cellular changes in autophagy, mitochondrial biogenesis, and lipid synthesis or transport. AD-associated genes identified by large GWAS studies are significantly overrepresented in differentially expressed genes in cells lacking HS synthesis. We also show that reducing HSPG-mediated signaling affects mitochondrial function, autophagy, and lipid metabolism in *Drosophila* in a manner that counters deficits produced by *presenilin* knockdown and can suppress cellular phenotypes and molecular signatures in animals with compromised *presenilin*.

RESULTS

Transcriptomics of human Hep3B cells defective in HS synthesis shows broad effects on the expression of genes affecting lipid metabolism, autophagy, mitochondria, and AD-associated genes

We have previously reported that reducing heparan sulfate synthesis or modification alters autophagy flux and both function and morphology of mitochondria.[20,21,26] Reducing HS biosynthesis can suppress mitochondrial dysmorphology and muscle cell loss in a fly model of Parkinson disease achieved by mutations affecting *parkin*, the fly homolog of human *PARK2*. To determine if HS synthesis serves a conserved role in cellular and molecular events associated with AD pathology, we conducted RNA sequencing (RNA-seq) profiling of a human cell line (Hep3B) bearing loss-of-function mutations in *EXT1*,[27] a gene required for HS polymerization. Although this hepatocyte-derived cell line does not represent a cell type directly involved in AD, lipid metabolism and transport are a vital and conserved function implicated in AD, and these cells provide the means of exploring regulatory networks affected by heparan sulfate biosynthesis. A large number of differentially expressed genes was evident, with 1,949 genes showing increased expression and 1,294 with decreased expression in *EXT1*−/− cells ($p < 0.05$, FC ≥ 2.0). We examined genes involved in key cellular processes affected in AD, including autophagy, lipid metabolism, and mitochondria biogenesis and function.

Key components of lipid metabolism are represented in the statin drug pathway (https://www.wikipathways.org/instance/WP430) and provide a broad gene set for assessing differential gene expression affecting lipid. Four gene products in this pathway provide critical functions in the biosynthesis of cholesterol: (1) HMG-CoA reductase (3-hydroxy-3-methyl-glutaryl-coenzyme A reductase (HMGCR), the rate-limiting enzyme in the mevalonate pathway; (2) farnesyl-diphosphate farnesyltransferase 1 (FDFT1), the first specific enzyme in cholesterol biosynthesis, catalyzing the dimerization of two molecules of farnesyl diphosphate in a two-step reaction to form squalene; (3) squalene monooxygenase (also called squalene epoxidase, SQLE), catalyzing the first oxygenation step in sterol biosynthesis and considered one of the rate-limiting enzymes in this pathway; and (4) sterol O-acyltransferase 1, a resident enzyme of the endoplasmic reticulum that catalyzes the formation of fatty acid-cholesterol esters (SOAT1). Transcripts encoding all four of these key enzymes are dramatically and significantly reduced in *EXT1* KO Hep3B cells (Table S1), suggesting a significant suppression of cholesterol and cholesterol-ester biosynthetic capability. *SREBF2*, encoding a transcription factor that upregulates several genes affecting cholesterol biosynthesis, is significantly downregulated in *EXT1* KO cells. Other genes in this pathway involved in lipid transport/lipoprotein assembly are also significantly downregulated in *EXT1*−/− cells including *APOE*, *APOC2*, *APOC1*, and *APOB*. These proteins are involved in the export of lipids from lipid stores into the bloodstream and tissues. Another gene

affecting lipid transport[20,21] (MTTP), a protein required for the assembly of β-lipoprotein synthesis and lipid export from cells, is also markedly downregulated in *EXT1−/−* cells.

APOA4, encoding a protein promoting the transport of cholesterol from peripheral tissues to HDL, is upregulated in *EXT1−/−* cells. Other lipid transporters with an increased expression upon knockout of *EXT1* include *ABCA7*, *ABCA10, and ABCA12. ABCA7* is notable for the strong linkage of variants in genome-wide association study (GWAS) analysis with AD susceptibility,[28,29] and loss-of-function alleles are associated with an increased risk of AD in both European- and African-descent populations.[30,31] Another gene of interest in lipid biology is *PCSK9*, which encodes a regulator of low-density lipoprotein (LDL) receptor levels on the cell surface by altering intracellular trafficking. PCSK9 inhibitors are now FDA-approved drugs for lowering LDL levels in plasma. This gene is significantly downregulated in *EXT1* KO cells. MFSD2 lysolipid transporter A (MFSD2A), another gene affecting lipid transport, is dramatically reduced in expression levels in *EXT1−/−* cells. Mice with targeted knockout of *MFSD2A* are leaner and have reduced serum, hepatic, and adipocyte triglyceride levels.[32] It is intriguing that in the brains of the APP/PS1 mice, expression of the proprotein convertase subtilisin/kexin type 9 (PCSK9) and apolipoprotein E (APOE) were all elevated,[33] and both PCSK9 and APOE are reduced in the Hep3B *EXT1* KO cells.

Recent work has provided additional evidence that lipid accumulation is a critical element of AD pathogenesis.[34] Single-nucleus RNA sequencing (RNA-seq) analysis of brain cells isolated from AD and control samples revealed changes in gene expression that identified a class of microglia cells overrepresented in AD brains. These disease-associated microglia are notable for their increased expression of *ACSL1*, acyl-CoA synthetase long-chain family member, encoding an enzyme essential for lipid droplet biogenesis. Other genes affecting metabolic state, *NAMPT* and *DPYD*, are also elevated.[34] We find that all three of these genes indicative of an altered lipid metabolic state in AD-associated microglia are significantly downregulated in *EXT1−/−* Hep3B cells (see Table S1, *ACSL1*, log2 fold change = −1.2, p adj = $9.96e^{-35}$). These data emphasize the critical role HS-modified proteins have in lipid metabolism, including the formation of intracellular lipid stores, lipid droplets. The gene expression changes in cells lacking heparan sulfate biosynthesis are all in the direction of countering the changes seen in AD.

Earlier work showed that reducing heparan sulfate chain elongation or sulfation results in increased autophagy flux to the lysosome in *Drosophila*.[20,21] Genes critical for autophagy function are significantly elevated in *EXT1* KO cells compared to controls, including *SQSTM1*, *ULK1*, *PINK1*, *ATG9B*, *SRC*, and *PRKAG2*. GSEA of Hep3B *EXT1* KO compared to Hep3B+/+ cells also suggests activation of autophagy. Reactome pathways, selective autophagy, and aggrephagy are enriched (false discovery rate [FDR] = 0.24, and 0.25, respectively) and several other related gene sets show similar levels of increased component expression (autophagy and lysosome vesicle biogenesis) (Table S3). Other pathways with downregulation of gene sets or changes with false discovery rate between 0.25 and 0.3 are provided in Tables S4 and S5.

PPARGC1A, a master regulator of mitochondrial biogenesis, and *CHD9*, a coactivator of *PPARGC1A*, were significantly increased in *EXT1−/−* cells compared to controls. This is consistent with our data showing increased MitoTracker signal in *NDST1 −/−* cells (Figure 1) and MitoBlue in *EXT1 −/−* Hep3B cells (Figure 2). *PPARGC1A* is required for maintaining normal levels of mitochondrial gene expression and oxidative metabolism.[35] *PPARGC1A* also modulates gluconeogenesis and the capacity for cells to engage in glucose or fatty acid metabolism depending on nutrient availability.[36] *CHD9* is responsible for remodeling chromatin and is a coactivator of *PPARGC1A*.[37]

Effects of EXT1 knockout on Alzheimer disease susceptibility genes

AD is associated with changes in lipid metabolism and transport, and Hep3B cells are derived from hepatocytes, cells critical in these processes. We therefore were interested in differential gene expression profiles in Hep3B *EXT1−/−* cells-affected loci identified as AD susceptibility genes and their relation to functional gene groups implicated in AD pathogenesis. We selected genes identified by GWAS analysis classified at Tier 1 or Tier 2, reflecting different levels of association across six GWAS studies performed in populations of European ancestry and published since 2019[38] (Table S2). Overall, 46% of Tier 1 genes showed significant *EXT1*-dependent changes in expression, and Tier 2 representation among the differentially expressed genes was 57%. This reflects a statistically significant enrichment of AD-susceptibility genes among the differentially expressed genes affected by *EXT1−/−* in Hep3B cells (Chi-square with Yates correction, $p < 0.0001$). g:profiler assessment of the Tier 1 genes affected in *EXT1−/−* cells showed significant representation of amyloid precursor protein (APP) catabolic process (p-adjusted = 6.8×10^{-7}). These findings provide evidence for the capacity of heparan sulfate function to preferentially affect genes involved in AD susceptibility.

Large and significant downregulation was found for *FERMT2* and *APOE* (Table S2). *APOE* variants represent a substantial genetic risk for LOAD[39] and the discovery of the *ApoE3ch* variant that both rescues *PSEN1*-mediated EOAD and shows greatly reduced heparin binding suggests an important relationship between heparan sulfate function and AD pathology.[12] *FERMT2* encodes a scaffolding protein affecting integrin and TGF-β signaling and reducing expression in neural stem cells suppresses accumulation of phosphorylated Tau and extracellular APP-derived peptides.[40] Two other genes with differential expression in *EXT1−/−* cells include *BIN1* and *RIN3. BIN1* and *RIN3* interact directly and together affect Rab5-mediated endocytosis.[41] GWAS analyses have identified both as AD risk loci, and *RIN3* levels have been reported to increase in the hippocampus and cortex of APP/PS1 mice.[42] Elevated expression of *RIN3* in basal forebrain cholinergic neurons (BFCNs) from E16 embryos was associated with enlargement of early endosomes, suggesting an endocytosis abnormality. We have previously reported that compromising heparan sulfate biosynthesis increases activity-dependent endocytosis at the *Drosophila* neuromuscular junction,[43] and recent studies of tissue culture cells with compromised HS synthesis showed increases in endocytosis of GFP-tagged dextran, a measure of clathrin-dependent endocytosis (data not shown). These findings indicated that lowering heparan sulfate-dependent signaling can increase endocytosis, a process that is compromised in AD pathology.

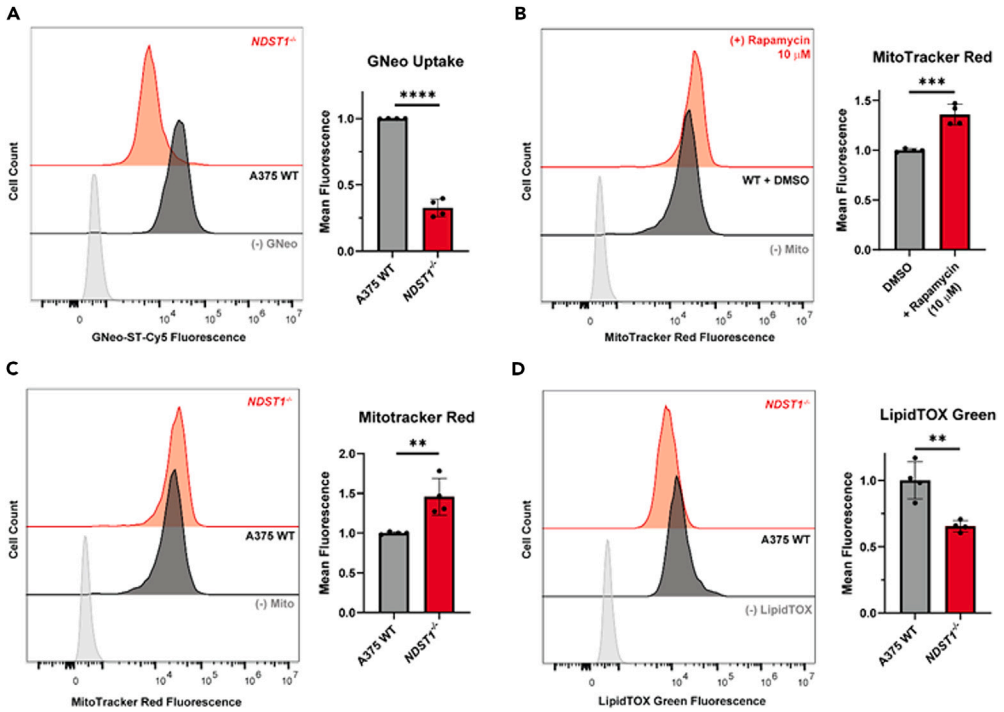

Figure 1. Flow cytometry analysis of A375 human melanoma cells with *NDST1* knockout

(A) Flow cytometry analysis of A375 wild-type and NDST1 knockout mutant (*NDST1*$^{-/-}$) cell lines after 1-h incubation at 37°C with biotinylated guanidinoneomycin (GNeo-biotin) conjugated to streptavidin-Cy5. NDST1 *N*-deacetylates and adds *N*-sulfate to glucosamine residues of heparan sulfate, which is required for GNeo binding[46] (t test, $n = 4$, ****$p < 0.0001$).

(B) Flow cytometry analysis of A375 wild-type cells after incubation with mTOR inhibitor, rapamycin (10 μM), for 24 h and subsequent 1-h incubation with MitoTracker Red. Rapamycin significantly increases the MitoTracker Red signal (t test, $n = 4$, ***$p < 0.001$).

(C) Flow cytometry analysis of A375 wild-type and *NDST1* mutant cells after 1-h incubation with MitoTracker Red (t test, $n = 4$, **$p < 0.01$).

(D) Flow cytometry analysis of A375 wild-type and *NDST1* mutant cells after a 30-min incubation at 37°C with LipidTox Green (t test, $n = 4$, **$p < 0.01$). All error bars represent SEM.

Conservation of heparan sulfate functions in mitochondrial and lipid metabolism in human cells and mouse astrocytes

We have examined the role of HSPGs in mitochondrial function and lipid metabolism in three different human-transformed cell lines as well as mouse primary astrocytes, derived from either wild-type mice or those bearing humanized variants of APOE that affect AD risk susceptibility in humans. Two independent and previously characterized human cell lines were examined: human melanoma A375 cells bearing CRISPR-mediated knockout of *NDST1*[44] and a hepatocellular carcinoma cell line, Hep3B, with a directed knockout of *EXT1*,[27] the cell line used for the transcriptomics analysis described earlier. Experiments were also carried out with HEK293T cells with lentiviral-mediated knockdown of either *EXT1* or *NDST1*. Mouse astrocytes were isolated from wild-type animals or those bearing humanized *APOE3* or *APOE4* variants.[45] Knockdown of *Ndst1* in these mouse astrocytes was achieved with transient lentiviral expression in culture.

Knockout of *NDST1* in A375 cells has a dramatic effect on the binding and internalization of GNeo, a modified neomycin analog with high affinity and specificity for heparan sulfate.[44] Fluorescence-activated cell sorting (FACS) measures of internalized GNeo of A375 *NDST1*−/− cells compared to wild-type A375 showed an approximately 3-fold reduction in internalized GNeo (Figure 1A). Autophagy induction has a profound effect on mitochondria levels, and the response of A375 cells to rapamycin, a TOR inhibitor, showed a significant increase in FACS measures of the mitochondrial marker, MitoTracker (Figure 1B). These data demonstrate this cell line displays a vigorous autophagy response. The effect of *NDST1*, and hence heparan sulfate structure, on mitochondria was assessed similarly using FACS analysis of MitoTracker levels, which increased 1.5-fold, comparable to the effects of rapamycin (Figure 1C). We have previously shown using transmission electron microscopy that A375 *NDST1*−/− cells have altered mitochondrial morphology,[26] and the MitoTracker results support the conclusion that compromising the structure of heparan sulfate has a profound effect on mitochondria. Induction of autophagy is also associated with reductions of intracellular neutral lipids, and we employed FACS analysis of LipidTOX staining to determine if the state of heparan sulfate affected lipid metabolism in A375 cells. LipidTOX level was significantly reduced in *NDST1*−/− cells compared to wild-type controls (Figure 1D).

The effect of heparan sulfate biosynthesis on mitochondria was also assessed in Hep3B cells, comparing wild-type to *EXT1* knockout cells. As observed for A375 cells with compromised *NDST1* function, eliminating the activity of EXT1, a chain-elongating heparan sulfate copolymerase, significantly increased the mitochondrial signal (MitoBlue, Figure 2A). Metric analysis of confocal images showed significant increases in mitochondrial number and size in *EXT1*−/− Hep3B cells compared to wild-type controls (data not shown).

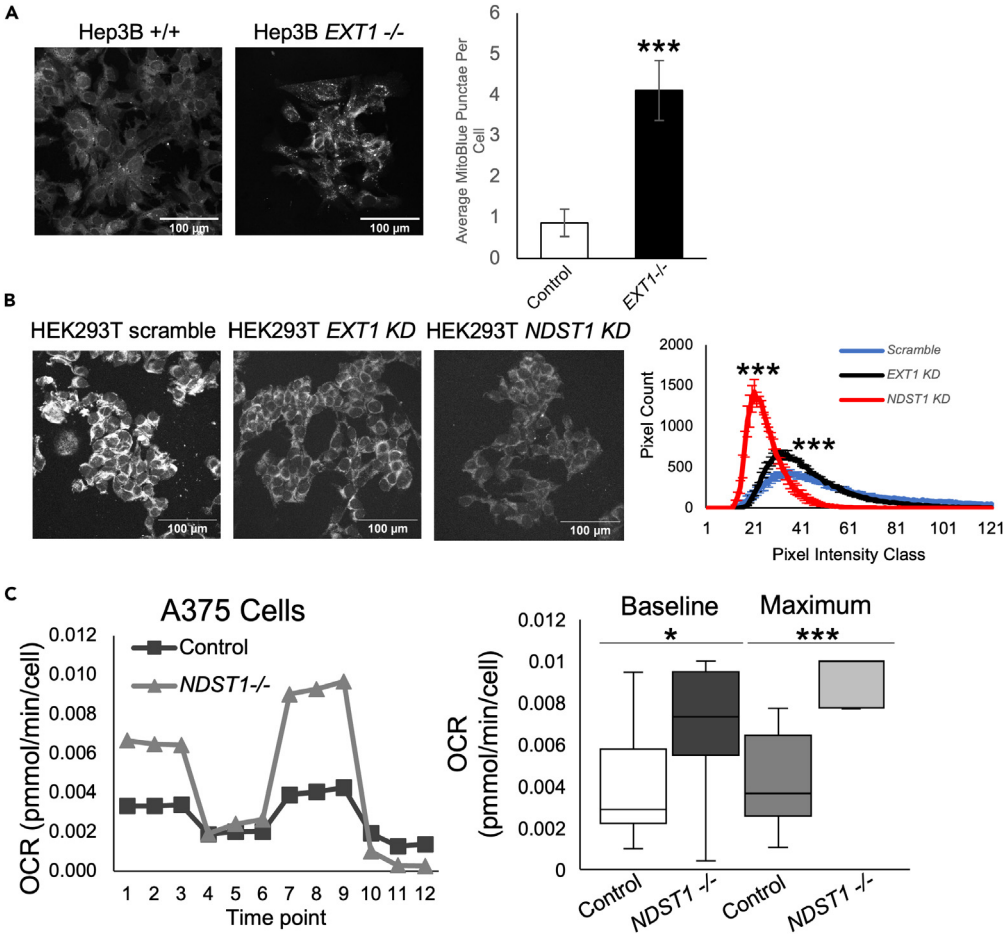

Figure 2. Reduced expression of heparan sulfate biosynthetic enzymes in human cell lines significantly increases mitochondria, reduces intracellular lipid droplets, and increases oxygen consumption rate measured by Seahorse Analyzer

(A) Representative confocal fields of Hep3B cells stained with MitoBlue fluorophore. Knockout of *EXT1* significantly increases the number of MitoBlue-positive punctae in Hep3B cells (t test, Hep3B EXT1+/+, $n = 17$ fields, Hep3B *EXT1*−/−, 19 fields; ***$p < 0.001$). Error bars show SEM.

(B) Representative confocal fields of HEK293T cells with stably integrated lentiviral vectors expressing scrambled (control), *EXT1*, or *NDST1*-directed RNAi. Intracellular lipid droplets assessed by staining with LipidTox Red. Graph shows average pixel intensity frequency distribution for the three HEK293 cell lines shown. Knockdown of *EXT1* and *NDST1* significantly decreases LipidTox Red staining intensity in HEK293T cells (Kolmogorov-Smirnov test, ***$p < 0.001$). Graph shows pixel intensity averages for a sampled area with error bars representing the SEM. The experiment was conducted in quadruplicate.

(C) Representative graph and quantification of A375 cells undergoing a Mito Stress Test. Knockout of *NDST1* significantly increases the baseline and maximal oxygen consumption rate (OCR) of A375 cells (t test, $n = 30$ (10 wells x 3-time points) per genotype, *$p < 0.05$, **$p < 0.01$, ***$p < 0.001$). The first three time points were taken under baseline culture conditions, time points 4–6 after oligomycin addition, an ATPase inhibitor, time points 7–9 after FCCP addition, which disrupts the proton gradient, and time points 10–12 showing OCR after block of electron transport with rotenone and antimycin A addition. The experiment was conducted in triplicate. Box and whisker plot shown in right panel, outlier points (<Q1 minus 1.5 IQR, >Q3 plus 1.5 IQR) excluded.

HEK293T cells with integrated lentiviral vectors targeting *EXT1* or *NDST1* were used to evaluate the level of intracellular lipid when heparan sulfate elongation or sulfation was reduced (Figure 2B). LipidTOX staining was significantly lowered upon knockdown of either of these two heparan sulfate biosynthetic enzyme-encoding genes. This is notable as a change in the pixel intensity distribution toward a greater representation of low-intensity pixels upon *EXT1* or *NDST1* knockdown compared to a scramble sequence lentiviral vector (Figure 2B).

The results described earlier document morphological changes for markers of mitochondria and neutral lipids stored in intracellular lipid droplets upon reduction of key heparan sulfate biosynthetic enzyme-encoding genes. To assess the functional consequences of changes in heparan sulfate levels or structure on mitochondria, oxygen consumption rates were measured with a Seahorse analyzer and a mitochondrial stress test. This test provides a measure of both baseline and maximal respiratory capacity. Significant increases in both baseline and maximal respiration rates were observed for A375 *Ndst1*−/− cells compared to wild type A375 (Figure 2C) and Hep3B *Ext1*−/− compared to wild-type Hep3B (Figure S1). These findings demonstrate that heparan-sulfate-modified proteins have a functional impact on the activity of mitochondria, with loss or partial loss of heparan sulfate biosynthesis increasing mitochondrial respiratory capacity.

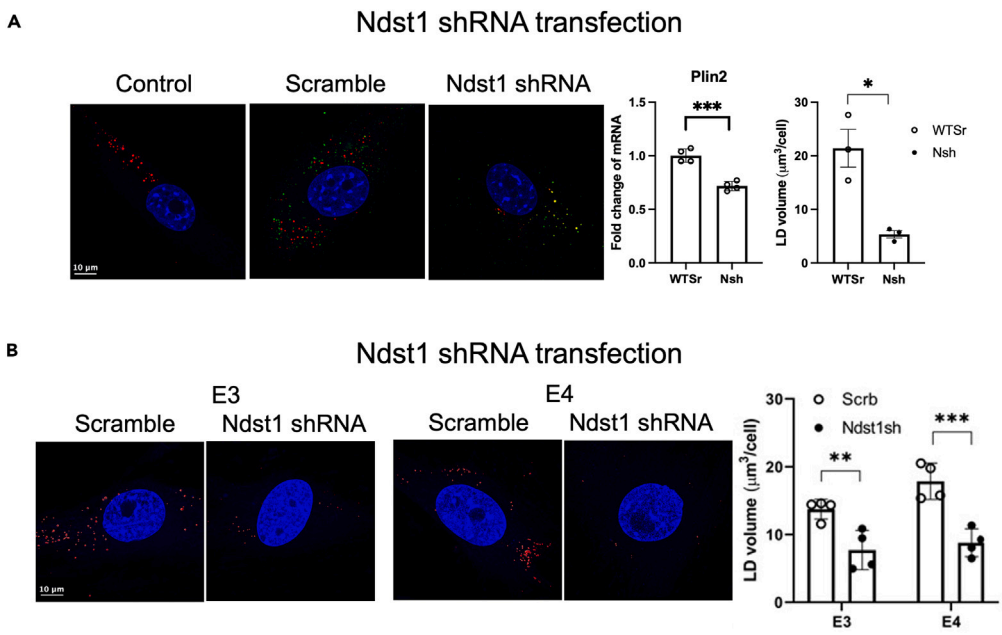

Figure 3. Knockdown of *Ndst1* in primary mouse astrocytes lowers levels of intracellular liposomes

(A) Micrographs showing levels of lipid droplets (LD), a marker for lentiviral transfection (green), and nuclear stain (DAPI, blue) in control, cells transfected with either a scramble sequence shRNA vector or one targeting *Ndst1*. *Ndst1 shRNA* produced reduced levels of LD number and volume (panels on the right), as well as decreases in *Plin2* expression measured by qPCR.

(B) The effect of *Ndst1 shRNA* was evaluated on astrocytes from animals expressing humanized variants of *APOE3* and *APOE4*. LD volumes were significantly reduced by *Ndst1* knockdown compared to scramble controls in astrocytes from either of these two genotypes [images show individual cells, nuclei (blue), and LD (red), and graphs provide quantitation of LD volumes. *$p < 0.05$, **$p < 0.01$, ***$p < 0.001$). Error bars represent SEM.

Knockdown of Ndst1 in mouse astrocytes reduces intracellular lipid levels

To evaluate the capacity of heparan sulfate to modulate attributes in cells affected by AD pathology, we examined intracellular lipids in wild-type mouse astrocytes as well as those expressing humanized *APOE3* and *APOE4* variants. Previous work has shown that astrocytes provide important metabolic support for neurons, and APOE variants affect this important capacity.[45] Astrocytes expressing the APOE4 variant showed elevated accumulation of intracellular lipid compared to wild-type or APOE3-expressing cells. Knockdown of *Ndst1* (to 60% of wild-type levels, measured by qPCR) using a lentiviral vector reduced intracellular lipid significantly in wild-type astrocytes, representing a greater than 4-fold reduction in lipid droplet volume (Figure 3A). This was accompanied by significant reductions in *Perilipin 2* mRNA, the gene encoding a protein localized to the phospholipid shell of lipid droplets, compared to astrocytes transfected with a lentivirus bearing a scrambled sequence (Figure 3A). Lentivirus-directed knockdown of *Ndst1* in astrocytes from mice expressing humanized *APOE3* and *APOE4* variants both display comparable and significant reductions in intracellular lipid compared to controls expressing a scrambled sequence lentivirus (Figure 3B).

Presenilin/Psn deficit in Drosophila neurons produces degeneration suppressed by reducing heparan sulfate modification

Presenilin is one component of an enzyme complex, γ-secretase, a protease with a number of important substrates, including amyloid precursor protein (APP) and Notch.[47,48] Mutations affecting *presenilin-1 (PS1)* function are responsible for a familial, early onset form of AD. Although *PS1* mutations show dominant inheritance, these variants are loss or partial loss-of-function variants, established by the demonstration that approximately 90% of 138 mutant proteins derived from human-disease-associated variants and reconstituted into an active enzyme complex showed reduced Aβ peptide production.[11,49] These studies demonstrate that *PS1* partial loss-of-function models are relevant to understanding AD mechanisms. In vertebrate systems, compromising presenilin function results in mitochondrial dysfunction, accumulation of intracellular lipid, and disruption of autophagosome to lysosome trafficking.[50] With these observations in mind, the cellular and molecular phenotypes of partial loss of function changes in *Drosophila* γ-secretase were examined. These experiments were made possible by the development of effective RNAi constructs directed against two essential subunits of the γ-secretase complex, Presenilin (Psn), the catalytic subunit, and Nicastrin (Nct), an evolutionarily conserved component proposed to affect substrate selection.[51] All four protein components of human γ-secretase are represented in *Drosophila*, and these two homologous enzyme complexes share common substrates. RNAi knockdown of either *Psn* or *Nct* mRNAs in neurons produces neurodegeneration in the adult brain and retina and has effects even when functional changes are conditionally restricted to adult neurons.[52]

We began by assessing the phenotypic severity of three RNAi constructs, two different *Psn* and one *Nct*-directed UAS-RNAi vector expressed in the brain using a neuron-specific *Gal4* driver, *elav-Gal4*. Animals were evaluated for a startle-induced negative geotaxis assay

(Figure 4E), a locomotor reactivity response where animals move upward after a gentle tapping to the bottom of a plastic tube.[53] These findings confirmed previously published phenotypes, with *shPsn2* showing more severe behavioral deficits and *shPsn3* demonstrating a modest but significant deficit in behavior when compared to controls (Figure 4E, *shPsn3* data shown). Expression of *Nct* RNAi in neurons when animals were reared at 25°C was nearly completely lethal. The majority of the analyses described below therefore focused on *shPsn3*, the RNAi construct with an intermediate phenotype.

Earlier work has shown the capacity of reduced heparan sulfate biosynthesis to suppress cell degeneration, restore dysmorphic mitochondria, and reduce accumulation of ubiquitin-modified proteins in *parkin* mutants, a *Drosophila* model of *PARK2*-mediated Parkinson disease.[21] Partial reductions in the function of either of two genes involved in heparan sulfate biosynthesis, *sulfateless (sfl)*, encoding a homolog of *N*-deacetylase *N*-sulfotransferase (NDST1), or *tout velu (ttv)*, a glycosyl transferase responsible for heparan sulfate chain elongation (homolog of human *EXT1*), had dramatic effects on *parkin* mutants, restoring muscle cell morphology and flight activity.[21] We, therefore, examined the capacity of reduced heparan sulfate biosynthesis to affect neurodegeneration in the brain of *shPsn3* RNAi-expressing animals. Adult flies expressing *shPsn3* RNAi under the control of *elav-Gal4* were aged for 7 or 30 days prior to phalloidin and Hoechst staining of adult heads to visualize actin and nuclei in whole-brain preparations.[54] Serial confocal sections of the entire brain were taken to identify vacuoles, areas of acellularity produced by neuronal loss (Figure 4A, white arrows). Consistent with earlier published work, expression of *shPsn3* in the adult brain produced a marked increase in neurodegeneration measured as the area of vacuolization or number of vacuoles per brain compared to control animals expressing a w^{RNAi} construct (the *white* gene governs eye pigmentation) (Figures 4A and 4B). Knockdown of *sfl* transcripts with a sfl^{RNAi} construct showed no difference from control animals with respect to levels of degenerative vacuoles. However, RNAi of *sfl* significantly reduced the level of degeneration in the brain mediated by *shPsn3* knockdown in animals aged 7 or 30 days (Figure 4B, compare *shPsn3* to *shPsn3;*sfl^{RNAi}). These findings demonstrate that *Psn* neurodegenerative phenotypes can be suppressed by modest reductions in *sfl* function and hence HSPG-mediated activities.

Disturbed *presenilin* function in *Drosophila* produces an elevated level of apoptosis,[55] reflecting activities observed in human cells bearing *PSEN1* mutations.[56,57] We therefore explored the capacity of reduced *sfl* function to suppress apoptosis mediated by *Psn* knockdown. A fluorescent vital dye, acridine orange (AO), is a widely used marker for apoptosis in *Drosophila*[58] and vertebrate cells[59] and provided a clear indication of elevated apoptosis in adult brains with *Psn* knockdown (Figures 4C and 4D). The level of AO-positive cells was dramatically reduced in *shPsn3* animals with coexpression of sfl^{RNAi} in neurons, reflecting a remarkable capacity of reduced HS sulfation to abrogate apoptosis in adult brains (Figures 4C and 4D). Behavioral assessment of adult animals also showed suppression of *presenilin* knockdown-mediated defects by reducing *sfl* mRNA levels. *shPsn3;*sfl^{RNAi} animals performed significantly better in the geotaxis assay than *shPsn3* but were not restored to control levels (Figure 4E).

Cellular processes regulated by Psn and heparan-sulfate-modified proteins

The capacity of reduced *sfl* function to rescue neurodegeneration and behavioral deficits mediated by *presenilin* deficits prompted an analysis of cellular phenotypes with a focus on mitochondria, intracellular lipid, and autophagosome-related structures, all features known to be disrupted by *PS1* mutations in humans.[50,60] Given the documented effects of *PS1* mutations on many cell types and their involvement in conserved cellular functions, we examined the cellular phenotypes of *presenilin* and *sfl* knockdown in the larval fat body. The fat body is an essential metabolic regulatory organ where autophagy serves a critical role in balancing anabolic and catabolic processes.[61] It therefore serves as an ideal cell type to monitor conserved elements of lipid metabolism, autophagy, and mitochondrial function affected by *presenilin* and its modulation by heparan-sulfate-modified coreceptors. The fat body has also shown to be an integral element of mechanisms affecting aging,[62] a topic relevant to the studies here.

Fat body cells are large (~60 μm) polyploid cells where intracellular organelles can be visualized in detail with specific fluorescent markers using serial confocal microscopy. Genes affecting mitochondria and neurodegeneration, including *parkin* and *pink1*, have been identified using RNAi screens and visualization of mitochondria in fat body cells,[63] demonstrating the utility of this preparation for assessing cellular phenotypes relevant to neural function and disease. Selective knockdown of genes in fat body cells is possible using UAS-RNAi-producing transcripts expressed under the transcriptional control of *r4Gal4*, a fat-body-specific *Gal4* transgene. *r4Gal4* produces a reduction of *Psn* and *sfl* mRNA by 32% and 28% of levels measured in control animals (w^{RNAi}), respectively, determined by RNA-seq (see later discussion).

Psn and *sfl* knockdown in Drosophila fat body have opposing effects on mitochondrial structure and liposome organization

In order to evaluate the effect of presenilin function on mitochondria and intracellular lipids, *Psn*-RNAi expression was directed to the fat body. Mitochondria and intracellular lipids were visualized using the fluorescent probes MitoTracker Red and LipidTOX by serial confocal microscopy, respectively. *Psn* knockdown had profound effects on the level and morphology of MitoTracker-labeled organelles in fat body cells (Figures 5A and 5B). MitoTracker signal intensity was significantly reduced in *shPsn3* preparations compared to control animals expressing w^{RNAi} (Figure 5B). The size of MitoTracker-labeled organelles was also affected by *Psn* knockdown (Figure 5B), indicating that mitochondria are smaller upon reductions of *Psn* function. The effect of *shPsn3* on mitochondrial morphology was confirmed by transmission electron microscopy (TEM) and serial block face scanning electron microscopy (SBFSEM), revealing small, ellipsoid mitochondria in animals with *shPsn3*, compared to larger, branched mitochondria in control preparations (RNAi of *w* gene) or animals with sfl^{RNAi} (Figure 5E).

We have previously shown that reductions in heparan sulfate biosynthetic enzyme-encoding genes affect mitochondrial morphology in muscle, producing larger mitochondria via a process that requires an intact autophagy system.[21] We observe a similar phenotype with RNAi of *sfl* in fat body cells, with a more intense MitoTracker signal and larger, labeled structures compared to w^{RNAi} controls

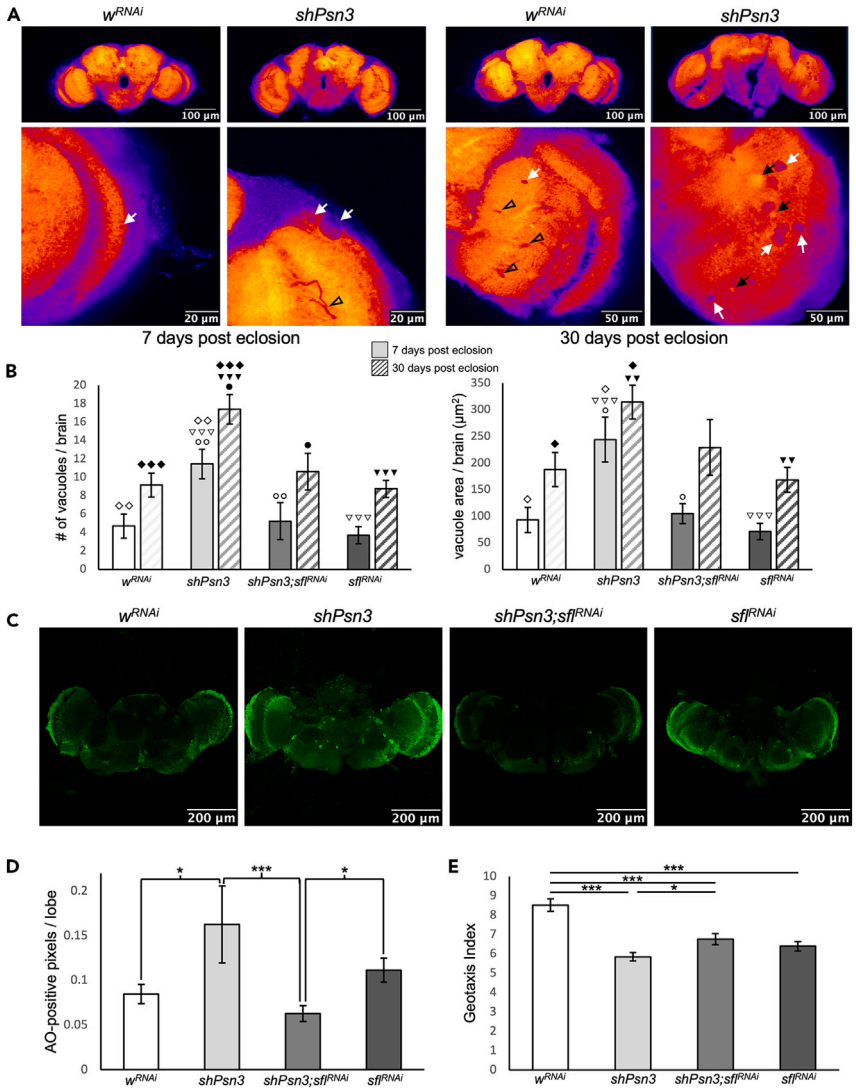

Figure 4. Reduction of *sfl* function reduces *Psn*-knockdown-induced neurodegenerative vacuole formation and apoptosis levels

(A) Representative images of *Drosophila* brains stained with Alexa Fluor 594-Phalloidin and imaged by confocal microscopy. Top row panels show low magnification images of the entire brain; bottom row: higher magnification (see scale bars). White arrows indicate neurodegenerative vacuoles. Black arrows indicate flares showing the higher staining intensity of phalloidin associated with and near vacuoles. Black arrowheads indicate tracheoles, air conducting tubules, discernable in the serial confocal sections.

(B) Bar graphs showing average vacuole area and count per brain in female *Drosophila*. Vacuole area and number of vacuoles per brain are significantly increased in *shPsn3* animals compared to controls and significantly elevated compared to *shPsn3;sfl*^{RNAi} animals 7 days post-eclosion (ANOVA Tukey test: w^{RNAi} $n = 10$, *shPsn3* $n = 24$, *shPsn3;sfl*^{RNAi} $n = 14$, sfl^{RNAi} $= 20$; $*p < 0.05$, $**p < 0.01$, $***p < 0.001$); error bars represent standard error of the mean (SEM). Open symbols denote significance values for 7-day-old animals and closed symbols for 30-day-old animals. Number of symbols indicates levels of significance between the two groups with those symbols. Vacuole area and number of vacuoles per brain are significantly increased in *shPsn3* animals 30 days post-eclosion compared to controls, and double *shPsn3;sfl*^{RNAi} animals showed a significant reduction in vacuole number compared to *shPsn3*. Vacuole area was reduced in *shPsn3;sfl*^{RNAi} animals compared to *shPsn3* but did not achieve significance (ANOVA Tukey test: w^{RNAi} $n = 13$, *shPsn3* $n = 20$, *shPsn3;sfl*^{RNAi} $n = 8$, sfl^{RNAi} $= 20$; $*p < 0.05$, $**p < 0.01$, $***p < 0.001$).

(C) Representative images of *Drosophila* brains stained with the apoptosis marker, acridine orange. Micrographs are pixel maximum intensity stacks from confocal serial sections.

(D) Bar graphs quantifying apoptotic staining in optic lobes of adult female *Drosophila*, age matched 1–3 weeks. Apoptosis is significantly higher in *shPsn3* than controls (w^{RNAi}) and significantly lower in *shPsn3;sfl*^{RNAi} compared to *shPsn3* animals (ANOVA Tukey test: w^{RNAi} $n = 10$, *shPsn3* $n = 10$, *shPsn3;sfl*^{RNAi} $n = 10$, sfl^{RNAi} $n = 10$; $*p < 0.05$, $**p < 0.01$, $***p < 0.001$).

(E) Bar graphs demonstrating average performance on negative geotaxis assays in adult female *Drosophila*, aged 4–7 days. Performance is statistically significant between w^{RNAi} and all other genotypes (ANOVA Tukey test: w^{RNAi} $n = 25$, *shPsn3* $n = 20$, *shPsn3;sfl*^{RNAi} $n = 25$, sfl^{RNAi} $= 35$; $*p < 0.05$, $**p < 0.01$, $***p < 0.001$). *shPsn3;sfl*^{RNAi} show significantly improved geotaxis compared to *shPsn3* animals ($p < 0.05$).

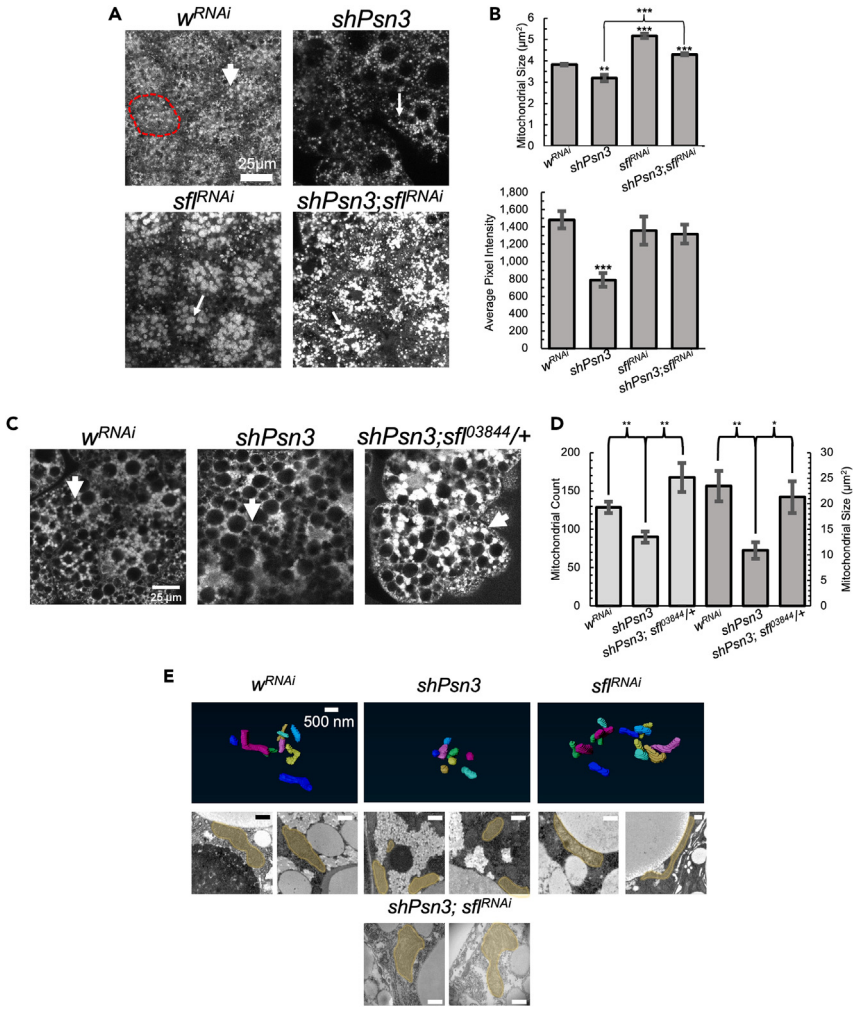

Figure 5. *psn* and *sfl* function alter mitochondrial number and morphology in fat body cells, and *sfl* knockdown suppresses psn^{RNAi}-mediated abnormalities

Mitochondria labeled with MitoTracker Red and visualized by confocal serial section.

(A) Images are projections of a stack of confocal images, showing the organization and morphology of mitochondria. The red dashed circle indicates the margins of one cell. White arrows mark individual mitochondria. Spheroid-shaped areas without MitoTracker Red signal are the large liposomes found in fat body cells.

(B) The measure of mitochondrial size shows *Psn* knockdown significantly reduces the size of MitoTracker-positive structures compared to controls (w^{RNAi}), whereas sfl^{RNAi} has the opposite effect (increased size of MitoTracker-positive structures); error bars represent SEM (t test, *p* values are in relation to w^{RNAi} except where marked by bracket, $^{**}p < 0.01$, $^{***}p < 0.001$). sfl^{RNAi} rescues the mitochondrial phenotypes produced by *psn* knockdown, reflected both in morphology and size of MitoTracker-labeled structures (*p* values in relation to w^{RNAi}, $^{***}p < 0.001$). Significant differences were also measured for pixel intensity, with *shPsn3* showing reduced average pixel intensity compared to controls and sfl^{RNAi} *shPsn3* animals restoring pixel intensity to control levels (w^{RNAi}).

(C) Reducing *sfl* function with a characterized P element mutant, sfl^{03844} also rescues mitochondrial number and morphology in fat body cells with *Psn* knockdown. Mitochondria labeled with MitoTracker Red and shown in a single optical confocal section (individual mitochondria marked with arrow).

(D) Measures of mitochondrial count and size shows *Psn* knockdown significantly reduces the size and number of MitoTracker-positive structures compared to controls (w^{RNAi}), whereas sfl^{RNAi} significantly increases the size and number of MitoTracker-positive structures compared to *Psn* knockdown (t test, $n = 10$, $^{*}p < 0.05$, $^{**}p < 0.01$).

(E) Top row panels show serial block-face EM assembly of mitochondria, providing a 3D rendering of mitochondrial morphology. Mitochondria in *shPsn3* are small spheroidal structures, whereas both control (w^{RNAi}) and sfl^{RNAi} show more elongated mitochondria. The TEM images in the second and third rows of images show mitochondria (highlighted in translucent color) in these genotypes. Of note is the very elongated mitochondrion found in a sfl^{RNAi} animal and the large, lobed mitochondrial found in sfl^{RNAi} *shPsn3* preparations.

(Figures 5A and 5B). SBFSEM and TEM confirmed the organization of mitochondria detected with MitoTracker in sfl^{RNAi} animals, with some large mitochondria evident in electron microscopic (EM) sections (Figure 5E).

The morphology of liposomes was evaluated by confocal microscopy of neutral lipid fluorophore staining (LipidTOX) as well as TEM. Control animals (w^{RNAi}) showed very regular liposomes, largely filling the entire cell (Figure 6A). *shPsn3* animals had larger, spherical liposomes

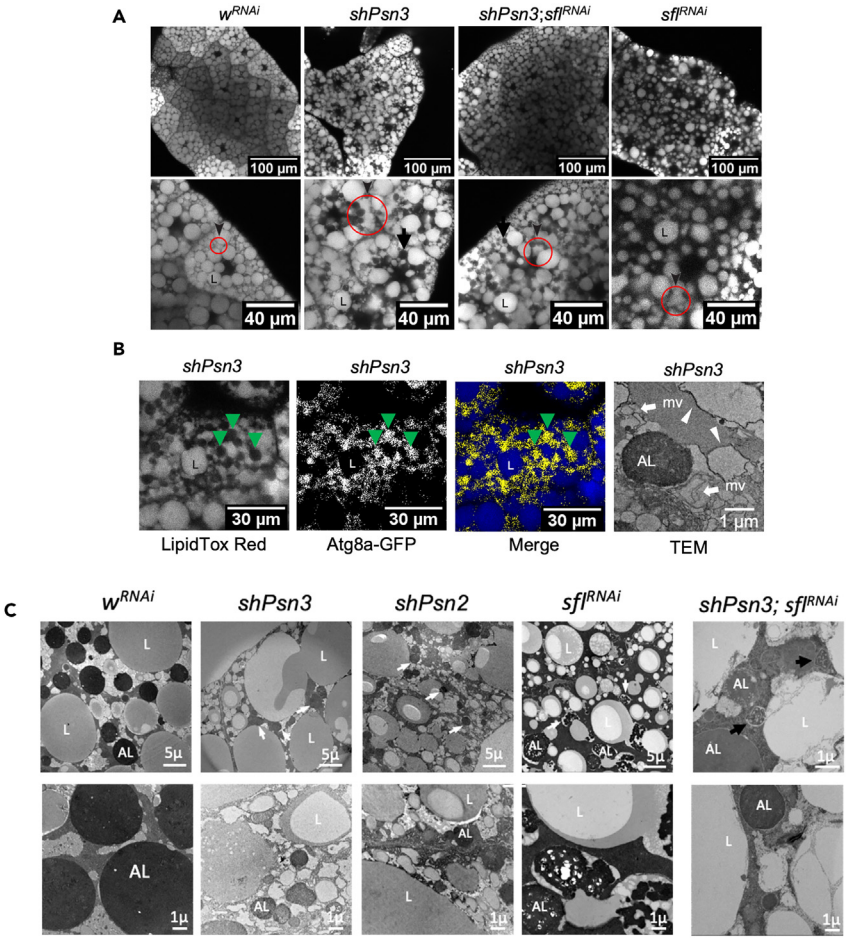

Figure 6. *sfl^{RNAi}* partially reverts *psn*-knockdown-induced alterations in liposome morphology

(A) Representative images of fat body stained with LipidTox Red. Top row shows lower magnification image, whereas lower row shows higher magnification, more detailed view. Control fat body cells (w^{RNAi}) show large, regular liposomes (L) filling the cell body. *shPsn3* results in changes in the spacing of liposomes and the appearance of irregularly shaped LipidTox staining structures (red circles and arrowheads). sfl^{RNAi} produces a reduced density of liposomes and also some irregularly shaped LipidTox staining structures. Arrows indicate vesicular-shaped gaps in the LipidTox Red signal (see details in C). The letter "L" labels liposomes.

(B) Fat body cells stained with LipidTox in animals expressing *Atg8a-GFP* transgene and *shPsn3*. The vesicular structures devoid of LipidTox staining show a GFP signal, indicating an accumulation of Atg8a (green arrowheads). The far-right panel shows a TEM micrograph of a *shPsn3* fat body cell with double membrane structures (white arrowheads), consistent with autophagosome morphology (relatively electron-lucent compared to autolysosomes [AL] as well as multi-vesicular bodies (arrows). These structures are found in fat body cells with compromised autophagy flux.[64]

(C) TEM micrographs of fat body cells, showing the organization of autolysosomes (ALs) and liposomes (L). ALs appear as electron-dense structures, 2–5 µm in control animals (w^{RNAi}) but smaller and less electron-dense in animals with RNAi of *Psn*. Shown are TEM images from two independent *Psn* RNAi lines (*shPsn2*, *shPsn3*). Smaller ALs indicated by white arrows. In sfl^{RNAi} animals, ALs display a different appearance, with electron-dense "cables" within a structure that can be seen fused with liposomes in some cases. Two micrographs of *shPsn3*,sfl^{RNAi} preparations are shown (both higher magnification), with some restoration of AL size and electron density, as well as the appearance of ALs fusing with liposomes (black arrows) as seen in sfl^{RNAi}.

with an increase of irregularly shaped lipid-staining structures (Figure 6A, red circled structures) compared to the control. TEM confirmed the presence of large and some fused liposomes in *shPsn3* animals (Figure 6C). Also apparent were spherical structures smaller than liposomes, intermixed among them, and evident by their absence of staining (Figure 6A). These structures were not prevalent in control or sfl^{RNAi} animals. To determine the nature of these intracellular organelles, we examined the distribution of an autophagosome marker, GFP-Atg8a (Figure 6B). Staining with both LipidTOX and GFP-Atg8a showed these features to be Atg8a-positive and hence derived from an autophagosome-related organelle (green arrowheads, Figure 6B). The accumulation of these structures in *shPsn3* fat body cells indicates a change in autophagosome structure or traffic in animals with *Psn* knockdown. TEM sections from *shPsn3* animals also show an accumulation of double membrane organelles consistent with autophagosome morphology as well as multivesicular structures (Figure 6B). These are cellular phenotypes characteristic of limited autophagosome maturation[64] and further suggest that *Psn* knockdown compromises autophagy flux and results in an accumulation

of Atg8a-positive structures. *sfl*^{RNAi}*-expressing* animals also showed changes in liposome morphology, with a lower density of LipidTOX-staining structure compared to controls (Figure 6A) and a greater representation of smaller liposomes. These findings were confirmed by TEM analysis (Figure 6C).

PSEN1 deficits are known to disrupt autophagosome traffic, and this cellular abnormality is common to several neurodegenerative disorders. Conversely, reductions in heparan sulfate chain length or sulfation increase the trafficking of autophagosomes to the lysosome.[20] It was therefore of interest to examine autophagosome-related structures in fat body cells with *presenilin* or *sfl* knockdown. In TEM micrographs of wandering third-instar larvae fat body cells, autolysosomes are prominent structures with a characteristic size of 2–5 μm, a single encompassing membrane, and containing varied electron-dense materials.[64] These are readily seen in TEM sections of control cells (Figure 6C). In two different *Psn* RNAi-producing lines, TEM showed smaller, less electron-dense autolysosome structures, indicating that knockdown of *Psn* alters autophagy in these cells. *sfl*^{RNAi} had a very different effect on autolysosomes, producing a membrane bound structure with a network of electron-dense "cables" within. These autolysosomes were often seen in association with or having coalesced with liposomes (Figure 6C). These structures are consistent with the induction of autophagy and the liberation of lipids from liposomes in these animals.[65]

Reduction of *sfl* function suppresses cellular abnormalities mediated by *Psn* knockdown

The cellular changes mediated by *Psn* or *sfl* knockdown were distinct and in an apparently divergent manner for both mitochondrial and liposome morphology. Autophagy-related structures were also altered in different ways in *Psn* versus *sfl* RNAi-bearing animals. We examined these subcellular features in cells with reductions in both *Psn* and *sfl* and found a restoration toward wild-type morphology. Mitochondria were significantly larger, and MitoTracker signal levels were higher in the *shPsn3 sfl*^{RNAi} double RNAi compared to *shPsn3* alone (Figures 5A and 5B). The capacity of reduced *sfl* expression to rescue *shPsn3* deficits was confirmed by testing the capacity of a characterized null allele of *sfl*, *sfl*^{03844}, to also suppress mitochondrial phenotypes mediated by reduced *presenilin* function (Figure 5C). Likewise, the distribution of liposomes was restored in the double knockdown toward the wild-type pattern (Figure 6A). TEM supported the same conclusion with the appearance of nearly normal size autolysosomes along with those resembling those characteristic of *sfl* knockdown in the double *shPsn3 sfl*^{RNAi} knockdown. This collection of phenotypes demonstrated the block or reversal of cellular deficits mediated by loss of *Psn* function by compromising the activity of heparan-sulfate-modified proteins.

Transcriptomics signatures of *Psn*, *sfl*, and *Psn sfl* double knockdown show that *sfl* knockdown restores wild-type patterns for key metabolic regulatory genes

The capacity of reducing heparan sulfate function to rescue cellular abnormalities of *presenilin* deficits prompted a search for molecular signatures that accompany that rescue. This strategy could identify genes that are functionally important for the pathology mediated by *presenilin* knockdown. Quadruplicate samples of RNA were isolated from the fat body of climbing third-instar larvae of the following genotypes: *shPsn3*, *sfl*^{RNAi}, *w*^{RNAi} (controls), and *shPsn3;sfl*^{RNAi} double knockdown. Genes with significantly changed expression levels in either *shPsn3* or *sfl*^{RNAi} compared to *w*^{RNAi} controls were identified, and those with opposing directions of change were determined (Figure 7A). It is notable that the greatest number of genes with significant and opposite differential gene expression are downregulated in *shPsn3* (Figure 7B). For example, in the 200 genes with the greatest fold difference, 18 show opposite expression changes for the *shPsn3* down, *sfl*^{RNAi} up gene set and only one gene for *shPsn3* up, *sfl*^{RNAi} down group. This suggests that the capacity of *sfl* knockdown to rescue *Psn* deficits lies largely with the correction of *shPsn3* downregulated genes.

Twenty-six genes show this pattern of differential gene expression, significantly downregulated in *shPsn3* animals and upregulated in *sfl*^{RNAi}. The expression of this set of genes was normalized in the *shPsn3;sfl* double knockdown (Figure 7B). Gene set analysis of these genes using g:profiler or PANGEA revealed significant enrichment after correction for multiple testing in GO biological processes transmembrane transport and Reactome solute carrier (SLC)-mediated transporter (R-DME-425407, corrected *p* value = 9.079e-4). A sizable proportion (37%) of these genes whose expression is decreased with *Psn* knockdown and displayed corrected expression mediated by *sfl* knockdown are members of the solute carrier gene family (Figure 7C). CG42235 (*kumpel*) encodes a homolog of the SLC5A family of transporters, Na+-dependent monocarboxylate cotransporters. This family of SLCs in *Drosophila* includes *kumpel*, *rumpel*, and *bumpel*, and the latter has been directly demonstrated to transport both pyruvate and lactate.[66,67] Overexpression of *bumpel*, a gene expressed in largely the same glial cell set as *kumpel*, rescues autophagy defects and neuronal death in a *Drosophila* model of *C9orf72* neurodegeneration.[66] Two members of the *SLC2A* family of hexose transporters are also represented in the gene set rescued by *sfl*, CG33281, and CG7882. Three members of the *SLC22A* family were also downregulated in *Psn* knockdown animals and restored to normal levels of expression with *sfl*^{RNAi}. This group of carriers transports organic ions, including carnitine, a molecule critical for fatty acid transport and oxidation in mitochondria.[68,69] Another group of transcripts suppressed upon *Psn* knockdown and restored to wild-type levels by simultaneous reduction of *sfl* expression affect metabolic regulation broadly and includes *neuropeptide-like precursor 2 (Nplp2)*, *insulin-like peptide 5 (Ilp5)*, and *urate oxidase (Uro)*. There are genetic interactions between insulin-like pathway signaling and uric acid accumulation in *Uro* mutants, suggesting the gene expression changes in *Ilp5* and *Uro* may be functionally connected.[70] *Nplp2* has recently been shown to affect lipid transport and homeostasis, serving as an exchangeable lipoprotein in the hemolymph.[71] *Ilp5* encodes a member of the insulin-peptide family and affects a number of metabolic processes.[72] These results collectively show that modest reductions in *Psn* function have dramatic effects on genes affecting metabolic processes that can be countered by modulation of HSPG function.

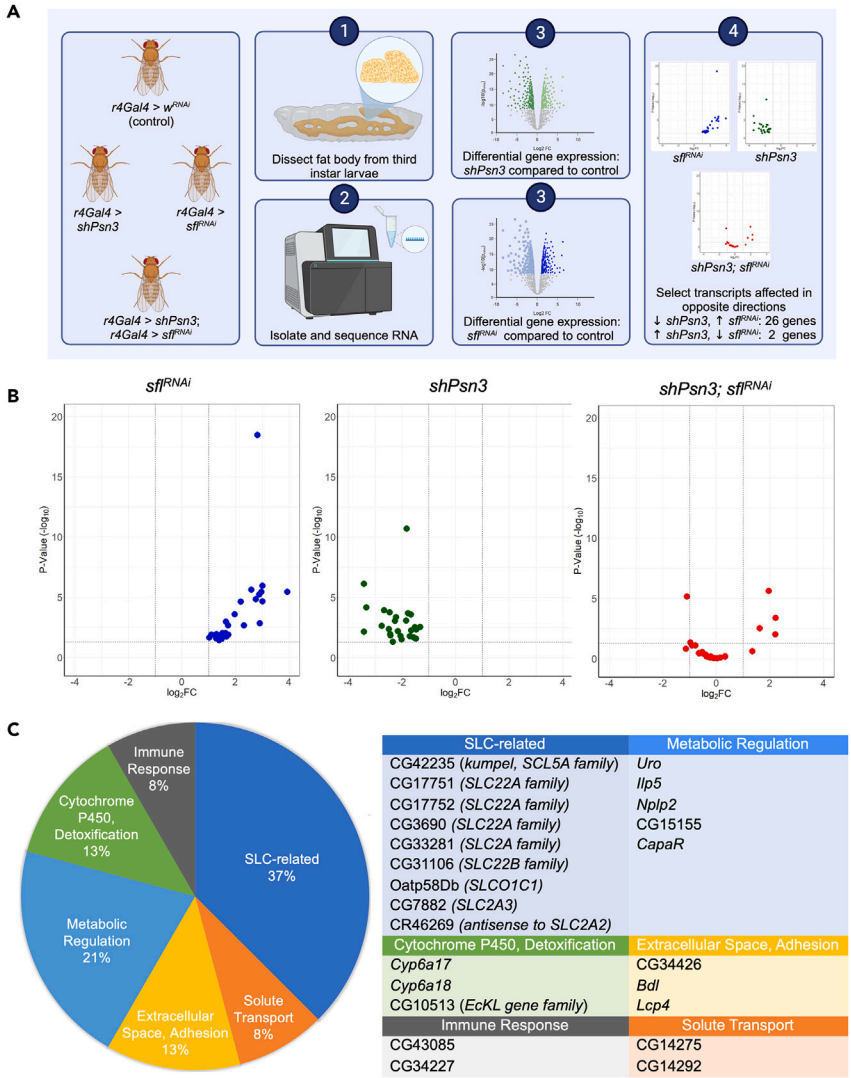

SLC-related	Metabolic Regulation
CG42235 (*kumpel, SCL5A family*)	*Uro*
CG17751 (*SLC22A family*)	*Ilp5*
CG17752 (*SLC22A family*)	*Nplp2*
CG3690 (*SLC22A family*)	CG15155
CG33281 (*SLC2A family*)	*CapaR*
CG31106 (*SLC22B family*)	
Oatp58Db (*SLCO1C1*)	
CG7882 (*SLC2A3*)	
CR46269 (*antisense to SLC2A2*)	
Cytochrome P450, Detoxification	**Extracellular Space, Adhesion**
Cyp6a17	CG34426
Cyp6a18	*Bdl*
CG10513 (*EcKL gene family*)	*Lcp4*
Immune Response	**Solute Transport**
CG43085	CG14275
CG34227	CG14292

Figure 7. RNA-seq analysis of fat body transcriptome shows *sfl*^{RNAi}-mediated reversal of a set of differentially expressed genes from *Psn knockdown* animals

(A) Experimental scheme for identifying differentially expressed genes with opposing changes in *shPsn3* versus *sfl*^{RNAi} and their expression in double *shPsn3;sfl*^{RNAi}.

(B) Volcano plots of genes significantly downregulated in *shPsn3* and upregulated in *sfl*^{RNAi} (y axis: probability of expression changes; x axis: fold change (FC) as $\log_2$. The far-right panel shows the volcano plot for those genes in the *shPsn3;sfl*^{RNAi} animals, demonstrating restoration of all but one gene to levels of control animals or higher.

(C) A breakdown of what genes show rescue of gene expression levels by functional class and listing of the affected transcripts, with their human homologs.

Transcriptome patterns affected by heparan-sulfate-modifying enzymes and comparisons between human and Drosophila cells

We have used a diverse set of systems and cells to understand how heparan-sulfate-modified proteins, via the fine structure of their glycosaminoglycan chains, affect cell processes known to participate in neurodegenerative pathophysiology. We have taken advantage of the broad conservation of these processes both across species and cell types. The transcriptome analysis conducted for a human hepatocyte-derived tumor cell line, Hep3B, bearing knockout of *EXT1*, a gene required for HS chain polymerization, provided a broad molecular confirmation of the changes observed with cellular markers of autophagy, mitochondria, and lipid metabolism. Knockdown of *sfl* in fat body cells in *Drosophila* provide a parallel system to evaluate the degree of conservation of these pathways and molecular signatures. Despite the differences between the cell types, as well as the genes targeted, *sfl/NDST* in *Drosophila* and *EXT1* in the Hep3B cells, there are shared cellular phenotypes as described earlier. The assessment of RNA-seq data from fat body cells with RNAi knockdown of *sfl* compared to control animals also provides some interesting and shared features relevant to vertebrate systems. Gene set analysis using the top 500 differentially

expressed genes from sfl^{RNAi} compared to controls (w^{RNAi}) revealed one functional human disease set that achieved significance (*p* value 0.04), neurodegenerative disease (Human Disease sets from FlyBase 2017). Pathway analysis among KEGG 2019 groups showed a number of metabolic pathways affected by knockdown of *sfl,* including glycerolipid metabolism (Adj. *p* value 0.007), metabolism of xenobiotics by cytochrome P450 (Adj. *p* value 2.5e-7), folate biosynthesis (Adj. *p* value 0.001), and galactose metabolism (Adj. *p* value 0.02).

A few individual genes with significant changes in expression are notable. *Spargel*, the *Drosophila* homolog of *PPARGC1A*, the master transcription regulator of mitochondrial biogenesis, is elevated in sfl^{RNAi} cells, providing a molecular signature for the effect of *sfl* on mitochondrial numbers. Genes affecting autophagy and membrane trafficking are also among those with significant changes, including *Cp1*, a homolog of mammalian *CSTL1*, that is significantly upregulated. *Cp1* in *Drosophila* is an important component promoting autolysosome clearance.[73] Genes affecting lipid accumulation are also altered in sfl^{RNAi} animals, the Dpp/TGB-β pathway in particular. In *Drosophila* this conserved signaling system suppresses lipid accumulation, and its downregulation is required for catabolic release of lipids.[74] The Dpp-activated transcription factor *Mad* is downregulated in sfl^{RNAi} fat body cells, as is a marker of Dpp-activity, *kek1*, indicators that Dpp signaling is reduced, a known heparan-sulfate-regulated pathway.[75,76] These gene expression changes are consistent with the morphological changes in liposomes observed in sfl^{RNAi} animals. Overall, the differential transcriptome signatures documented here indicate that heparan sulfate modification affects autophagy, lipid metabolism, and mitochondrial function across species and cell types.

DISCUSSION

A number of findings over the years have implicated heparan-sulfate-modified proteins in AD pathogenesis.[16,77] Recently, a dramatic example was reported for a member of a large kindred with a dominant disease-causing mutation in *PSEN1*.[12] This individual was cognitively intact well beyond the typical early onset of symptoms and was remarkable for being homozygous for a rare variant of *APOE3*, *APOE3 Christchurch*. This form of *APOE3* carries a mutation in the heparan-sulfate-binding domain, a change that essentially abrogated binding to heparin, a highly sulfated form of heparan sulfate. It was also reported in this study that heparin-binding strength for other disease-associated *APOE* variants was directly proportional to disease susceptibility (*APOE4>APOE3>APOE2>>ApoE3ch*). Recent work with mice bearing a humanized *APOE3ch* allele has provided evidence that the findings from that single individual are broadly applicable and point to a critical role for heparan sulfate function in *PSEN1*-mediated pathogenesis. The APOE3ch protein expressed in mice showed profound effects on microglial reactivity and Aβ-induced Tau seeding and spread.[13] Thus, the involvement of heparan-sulfate-modified proteins in PSEN1 and APOE function as well as AD pathogenesis seems evident. In this context, it is important to bear in mind the diverse and important functions served by heparan-sulfate-modified proteins. HSPGs serve to assemble protein complexes to modulate a number of cellular processes, including endo- and exocytosis as well as signaling at the cell surface, providing coreceptor function for a myriad of protein growth factors. How then do HSPGs participate and influence AD pathogenesis?

The studies reported here begin with exploring the relationship between heparan-sulfate-modified protein function and cellular and molecular signatures of AD pathogenesis in human cell lines and mouse astrocytes. We find that compromising heparan sulfate synthesis or modification has profound effects on autophagy, mitochondrial function, and lipid metabolism in these vertebrate systems. The changes in these cellular functions were reflected in heparan-sulfate-dependent changes in the transcriptome, including genes affecting cholesterol synthesis, lipid transport, autophagy, and mitochondrial biogenesis. There was also a remarkable enrichment of AD-associated genes identified by multiple GWAS studies in differentially expressed genes affected by loss of *EXT1*, a gene encoding a heparan sulfate polymerase. The cellular and molecular mechanism for HSPG modulation of AD-related changes was examined using a *Drosophila* model of *presenilin*-mediated pathology. The results from this analysis were clear: reducing heparan sulfate function increased autophagy, mitochondrial function, and biogenesis and lowered intracellular lipid droplets, as observed in human cells and mouse astrocytes. Furthermore, reducing heparan sulfate modification by partial loss of function of *sfl*, an *NDST1* homolog in *Drosophila*, rescued cellular and molecular abnormalities in *Psn*-defective animals, as well as the age-dependent neurodegeneration produced with partial reduction of *Psn* function.

The extensive genetic analysis of AD using GWAS, as well as whole-exome and -genome sequencing technologies, has made remarkable progress in identifying genes that confer susceptibility or causation of this disease. Collectively, these findings have identified shared genes and pathways affecting both familial, early onset as well as late-onset AD.[5,6] The current challenge is to identify the cellular and molecular events that are not only associated with disease but also serve a functionally critical role in pathogenesis. Model organisms provide the potential for addressing this challenge by virtue of the genetic tools that can identify genes that modify or suppress disease phenotypes. The conservation of the genes and their functions shown to be critical in AD in the fruit fly *Drosophila* provides an opportunity to identify functionally critical events in the molecular and cellular pathogenesis. This model system also allows for the study of interactions suggested by human genetic findings that have important implications for identifying potential targets for pharmaceutical intervention.

Transcriptome patterns and cellular events affected by heparan sulfate biosynthesis

Evaluating heparan-sulfate-dependent transcription patterns using Hep3B cells bearing an *EXT1* knockout was informative with regard to the pathways and cellular processes governed by HSPG-mediated signaling. First, it provided molecular evidence for the profound effects of HSPG function on cholesterol biosynthesis and lipid transport. These findings link the effects of reducing HS synthesis on intracellular lipids stored in liposomes that we have documented for a variety of cell types, including mouse astrocytes. We also observed effects on transcripts affecting mitochondrial biogenesis and autophagy, all processes involved in neurodegenerative disease. Finally, there was an enrichment of genes with differential expression affected by *EXT1* among AD-associated genes identified by extensive GWAS study. HSPG-controlled transcripts overlap to a remarkable degree with this set of genes implicated in the development and susceptibility to late-onset AD.

Functional analysis of several human cell lines and mouse astrocytes demonstrated that HSPGs serve critical functions in autophagy, mitochondrial physiology, and lipid metabolism. Modest changes in HS structure can produce marked changes in mitochondria, intracellular lipid, and autophagy flux. The changes affected by reducing heparan sulfate function counter the pathological shifts seen in AD and other neurodegenerative diseases, namely increases in autophagy, increased number and function of mitochondria, and lowered levels of intracellular lipid droplets.

We have used *Drosophila* to determine the functional interaction between *presenilin* and HSPGs as one model for evaluating the impact of HSPGs on neurodegeneration. In particular, the cellular and molecular phenotypes of reducing the function of the *Drosophila presenilin* gene, *Psn*, and a gene critical for heparan sulfate biosynthesis, *sfl*, were examined. Heparan-sulfate-modified proteins are known to regulate processes disrupted by *presenilin* deficits, autophagy in particular. In both *Drosophila*[20,21] and mice,[78,79] compromising the function of either heparan sulfate biosynthetic enzyme-encoding genes or individual heparan-sulfate-modified core proteins produces an increase in autophagy flux. For example, reductions in Perlecan (Hspg2) in mice has profound effects on autophagy,[78] as well as mitochondria and lipid metabolism,[79] events linked to changes in autophagy. In human hepatocellular carcinoma, elevated *Glypican-3* expression is associated with the suppression of autophagy, and reducing *GPC3* elevates autophagy levels and suppresses cell growth.[80–82] In contrast to the effects of lowering heparan-sulfate-modified protein function, mutations in *PSEN1* compromise autophagosome to lysosome flux,[83–86] and activating autophagy can restore autophagy levels and rescue mitochondrial abnormalities.[87] These findings point to the regulation of autophagy as a key element of AD pathogenesis and heparan-sulfate-modified proteins as an important determinant of autophagy flux.

Psn and *sfl* knockdown have opposing effects on key cellular processes, and modest reductions of *sfl* suppress *Psn*-mediated cell deficits and neurodegeneration

Previous work established that reductions in *presenilin/Psn* or *Nicastrin*, another component of the γ-secretase complex conserved in *Drosophila*, in adult neurons produce age-dependent degeneration.[52] We used this system to not only explore the interaction of *Psn* with heparan sulfate biosynthesis in neurodegeneration but also evaluate the cellular and molecular signatures in fat body cells, the principal metabolic storage and transport organ in *Drosophila*. *Psn* and *sfl* knockdown showed divergent effects on mitochondrial number and morphology, as well as intracellular lipid and autolysosome structure seen with EM and confocal visualization of fluorescent-tagged markers. Consistent with these different effects on cellular features, *sfl* knockdown was able to suppress both neurodegeneration and the spectrum of cellular phenotypes produced by partial loss-of-function *Psn* knockdown. It is notable that modest changes in the function of either of these genes produced readily discernable phenotypes. RNA-seq analysis of fat body cells with knockdown achieved with RNAi vectors showed 30%–40% reductions in mRNA and clear effects on cell phenotypes and cell loss in the nervous system.

Knockdown of *Psn* in fat body cells produced differential gene expression changes, as did sfl^{RNAi}. Comparing the differential expression patterns showed a subset of genes with opposite directions of change. The vast majority of these genes were downregulated in *Psn* knockdown animals and rescued to normal levels with simultaneous reduction of *sfl* mRNA levels. The identity of these genes, reflecting a molecular rescue signature, showed a large representation of solute carrier transporters, molecules inherently affecting metabolism and energy balance. One SLC family member was of particular interest, CG42235 (*kumpel*), encoding a homolog of the SLC5A family of transporters, Na^+-dependent monocarboxylate cotransporters. *Kumpel* and another member of this family, *bumpel*, have been shown to transport lactate and pyruvate[67] and when overexpressed, can rescue neuron loss mediated by expression of *C9orf72*, a human disease gene affecting frontotemporal dementia and amyotrophic lateral sclerosis.[66,88] Monocarboxylate and lipid transporters have also been shown to be vital in neuron-glia interaction in responding to reactive oxygen species (ROS) damage affected by mitochondrial dysfunction in neurons.[89] One gene affected by *Psn* knockdown and rescued by compromising HS sulfation is *Nplp2*, a lipid transport protein that responds to thermal stress, promoting survival.[71] *Nplp2* has functions that parallel *APOE* in vertebrate systems, namely serving as an exchangeable lipoprotein that can be soluble in hemolymph or blood and also associate with VLDLs.[71] Our transcriptomic analysis of *Psn* rescue by *sfl* has identified classes and gene family members shown to be critical in two other models of neurodegeneration in *Drosophila*. These findings emphasize the participation of HSPGs in cellular signaling systems affecting neuronal survival and point to processes critical in neurodegeneration, namely monocarboxylate and lipid transport.

HSPGs and AD pathogenesis

The experiments we have presented here assessing the role of HS structure on *presenilin*-mediated phenotypes in *Drosophila* have relied on reducing *sfl* mRNA. *sfl* is the sole *Drosophila* homolog of vertebrate *NDST* genes. *sfl/NDST* genes encode enzymes that remove an acetyl group and replace it with a sulfate on one of the two sugars that comprise the HS polymer, *N*-acetyl glucosamine. This sulfation step is critical for later sulfotransferase modifications and therefore serves as a means of broadly altering the sulfation pattern without altering chain length. The structure of heparan sulfate and its biosynthetic machinery are highly conserved across species, and structural analysis of *Drosophila* heparan sulfate has demonstrated its conserved sulfation patterns compared to vertebrate HS.[90,91] Indeed, a mouse *Ndst1* completely rescues *sfl* mutant phenotypes when expressed correctly from the endogenous *sfl* regulatory elements,[92] whereas mouse *Ndst2* has limited rescue activity. The 2-*O*, 6-*O* and 3-*O* sulfotransferases are conserved in *Drosophila* but the role of these modifications in autophagy, mitochondrial function, and lipid metabolism has not been investigated. HSPGs have been shown to affect the transcellular propagation of misfolded protein aggregates, and HS chain length and sulfation patterns do affect Tau, α-synuclein, and Aβ differentially although Tau appears to have the most stringent structural requirements.[93,94] Recently, it has been found that increases in 3-*O*-sulfated HS are found in AD brains.[95] These results support the identification of *HS3ST1* as an AD-associated risk gene and its role in Tau internalization.[96,97] It is worth noting that *NDST* activity is required for 3-*O* sulfation to take place.[98]

It has been known for some time that HSPGs are components of AD-pathological structures, namely neuritic plaques containing APP-derived peptides. Compromising HS biosynthesis reduces the levels of these pathological structures in mouse models of AD as does ectopic expression of HS degradative enzymes.[99,100] It is also known that HSPGs affect the internalization and propagation of Tau aggregates, providing structures that seed intracellular fibrils.[93] These studies all suggest mechanisms where HSPGs contribute to AD pathogenesis and therefore point to HS synthesis as a potential therapeutic target. The studies here provide another dimension; HSPGs affect signaling events that influence cellular processes known to be early and important for the development of neurodegenerative disease. Our studies show that HSPGs regulate autophagy, mitochondrial structure and function, and lipid metabolism, all important processes in neurodegeneration. We have provided direct evidence for HSPGs affecting neurodegeneration and cellular deficits mediated by reductions in *presenilin* function. HSPGs are cell surface signaling proteins, and their effect on *presenilin*-mediated cell defects indicates that changes in signaling are an important contributor to AD pathogenesis. It is intriguing that GSEA pathways with suppressed signaling in *EXT1−/−* cells are linked to aberrant signaling (Table S4: Signaling by PDGFR in Disease and Signaling by BRAF and RAF1 Fusions). Perhaps reducing heparan sulfate biosynthesis suppresses multiple signaling processes that promote AD pathogenesis.

Considerations of model systems to understand AD pathology

We have used a number of model systems to explore the function of heparan-sulfate-modified proteins in AD-related pathogenesis. These studies were prompted in some measure by human genetic findings on gene variants affecting *PSEN1*-mutation-mediated pathology, namely *APOE3 Christchurch,* which is remarkable for its lack of heparan sulfate binding and capacity to suppress cognitive decline. Nonetheless, it is important when using model systems to consider their relevance to the human disease. This is particularly true when the models are evolutionarily distant from humans, in organisms that do not normally exhibit the disease. These considerations apply to the work in fruit fly *Drosophila*, as well as cell types not directly involved in AD pathology. *Drosophila* do not show amyloid deposits or Tau accumulation unless directly engineered to do so. Yet, *presenilin* and all the other components of the γ-secretase complex are conserved between vertebrates and *Drosophila*, and deficits in *presenilin* produce similar cellular phenotypes, including mitochondrial deficits and increased apoptosis. Both of these cellular phenotypes were rescued by reductions of *sfl* function in *Drosophila,* assessed both in the brain and in a critical lipid regulatory organ, the fat body.

What can we learn about AD pathogenesis from cellular and molecular studies of non-CNS cell types, such as hepatocytes? For the work described here, the answer lies in the conserved mechanisms affected by both *presenilins* and heparan-sulfate-modified proteins. These molecules affect many cell types outside the nervous system but perform conserved regulatory functions. Cells that have a major role in lipid metabolism can be particularly instructive. This useful relationship has been noted by a number of studies, many focusing on the function of APOE, an important determinant of AD susceptibility.[101–103] There is also evidence that expression of APP restricted to the liver disrupts lipid metabolism and can produce some pathological features of AD, including increased neutral lipid accumulation and neurodegeneration.[104]

There is growing evidence that disturbances in lipid metabolism and APOE, a protein affecting lipid transport, are important elements of AD pathogenesis.[45] Recent work profiling transcripts using single-nucleus RNA sequencing from brain tissue of AD patients and controls bearing different *APOE* alleles is telling. AD-associated transcriptome signatures in microglia, were characterized by elevated levels of *ACSL1* expression, a gene affecting lipid droplet formation. These disease-associated microglia, called LDAM (lipid-droplet-associated microglia), were highest in AD patients with two APOE4 alleles. In addition, the levels of neutral, intracellular lipid were proportional to cognitive decline and anatomical extent of disease. The central role that lipid metabolism and APOE play in pathogenic processes argues that examining gene functions in other cell types, such as hepatocytes, that are also critical for the regulation and transport of lipid and express APOE can reveal important mechanistic relationships.

Limitations of the study

Some of the analysis of heparan sulfate influences on autophagy, mitochondria, and lipid was conducted in non-CNS human tumor cells or glycogen and lipid-storing cells in *Drosophila*. The relevance of these findings to AD pathogenesis in vertebrates is inferred based on conservation of these mechanisms across organisms and cell types.

STAR★METHODS

Detailed methods are provided in the online version of this paper and include the following:

- KEY RESOURCES TABLE
- RESOURCE AVAILABILITY
  - Lead contact
  - Materials availability
  - Data and code availability
- EXPERIMENTAL MODEL AND STUDY PARTICIPANT DETAILS
  - Mouse
  - Drosophila melanogaster
  - Human cell lines

- METHOD DETAILS
  - *Drosophila* brain dissection and assessment of neurodegeneration
  - Acridine orange brain staining of *Drosophila* adult brain[108]
  - Negative geotaxis assay
  - MitoTracker red staining of fat body
  - LipidTox red staining of fat body
  - Transmission electron microscopy
  - RNA isolation
  - RNA sequencing
  - RNA sequencing data analysis
  - MitoBlue staining of human cultured cells
  - LipidTOX red staining of human cultured cells
  - Preparation of fluorescently tagged guanidinylated neomycin-C5 conjugate and uptake experiments
  - MitoTracker red and LipidTOX green uptake studies and flow cytometry
  - Seahorse measurement of oxygen consumption rate
  - Isolation and culture of primary astrocytes
  - Astrocyte lipid droplets staining and quantification
  - Lenti-Ndst1shRNA transfection
  - RNA extraction and RT-qPCR from *Drosophila* and human cultured cells
  - LipidTOX staining
- QUANTIFICATION AND STATISTICAL ANALYSIS
  - Avizo image processing
  - *Drosophila* gene set analysis
  - Details of statistical tests

SUPPLEMENTAL INFORMATION

Supplemental information can be found online at https://doi.org/10.1016/j.isci.2024.110256.

ACKNOWLEDGMENTS

This work is supported by NIH/NIA grant (R21AG070843) and funding from the Penn State Eberly College of Science Lab Bench to Commercialization grant to S.B.S. R.J.W. is supported by NIGMS R35-GM150736. We also want to thank Missy Hazen and the Huck Institutes Microscopy Core facility for assistance with EM studies, the Huck Institutes' Flow Cytometry Core Facility for use of the BD LSRFortessa Special Order Research Product (SORP) and Dr. M. Rajeswaran for assistance with sample preparation. We also want to thank Grace O'Sullivan and Jolyn Toyomura for human cell line culture experiments, Uzair Alam for *Drosophila* culturing and *Nct* and *Psn* experiments, and Peter Mason and Tuyen Pham for coding and graphics expertise. We thank Maitreya Das, Deepro Banerjee, and Istvan Albert for their recommendations and assistance with the transcriptome analysis. We are indebted to Santhosh Girirajan for many helpful discussions and careful reading of the manuscript. Our thanks are extended to Teresa Niccoli for sharing of unpublished work and her thoughtful recommendations on the manuscript.

AUTHOR CONTRIBUTIONS

S.B.S. conceived the experiments in *Drosophila* and human cell systems, obtained the funding, and led the writing and editing of the manuscript. R.W. designed and supervised the FACS analysis and edited the manuscript. T.S. conducted the LipidTox FACS analysis. F.Y. and W.W. designed and conducted the mouse astrocyte experiments, contributed the corresponding figures, and edited the manuscript. N.S. conducted and designed both *Drosophila* and human cell line experiments, assisted in manuscript assembly and editing, and guided the efforts of A.C., A.K., R.B., R.M., S.S., M.O., M.R., L.S., and S.D. on both *Drosophila* and human cell line work. A.C. conducted the neurodegeneration experiments and contributed to manuscript assembly and editing.

DECLARATION OF INTERESTS

Dr. Selleck and The Penn State Research Foundation holds Patent No. 11053501 for Methods of Treating Neurodegenerative Disease by Inhibiting N-Deacetylase N-Sulfotransferase.

Received: January 30, 2024
Revised: May 6, 2024
Accepted: June 10, 2024
Published: July 2, 2024

REFERENCES

1. Alzheimer, A., Stelzmann, R.A., Schnitzlein, H.N., and Murtagh, F.R. (1995). An English translation of Alzheimer's 1907 paper, "Uber eine eigenartige Erkankung der Hirnrinde. Clin. Anat. *8*, 429–431. https://doi.org/10.1002/ca.980080612.
2. van Dyck, C.H., Swanson, C.J., Aisen, P., Bateman, R.J., Chen, C., Gee, M., Kanekiyo, M., Li, D., Reyderman, L., Cohen, S., et al. (2023). Lecanemab in Early Alzheimer's Disease. N. Engl. J. Med. *388*, 9–21. https://doi.org/10.1056/NEJMoa2212948.
3. Couzin-Frankel, J. (2023). Alzheimer's drug approval gets a mixed reception. Science *379*, 126–127. https://doi.org/10.1126/science.adg6275.
4. Sims, J.R., Zimmer, J.A., Evans, C.D., Lu, M., Ardayfio, P., Sparks, J., Wessels, A.M., Shcherbinin, S., Wang, H., Monkul Nery, E.S., et al. (2023). Donanemab in Early Symptomatic Alzheimer Disease: The TRAILBLAZER-ALZ 2 Randomized Clinical Trial. JAMA *330*, 512–527. https://doi.org/10.1001/jama.2023.13239.
5. Andrews, S.J., Renton, A.E., Fulton-Howard, B., Podlesny-Drabiniok, A., Marcora, E., and Goate, A.M. (2023). The complex genetic architecture of Alzheimer's disease: novel insights and future directions. EBioMedicine *90*, 104511. https://doi.org/10.1016/j.ebiom.2023.104511.
6. Kunkle, B.W., Grenier-Boley, B., Sims, R., Bis, J.C., Damotte, V., Naj, A.C., Boland, A., Vronskaya, M., van der Lee, S.J., Amlie-Wolf, A., et al. (2019). Genetic meta-analysis of diagnosed Alzheimer's disease identifies new risk loci and implicates Aβ, tau, immunity and lipid processing. Nat. Genet. *51*, 414–430. https://doi.org/10.1038/s41588-019-0358-2.
7. Wingo, T.S., Liu, Y., Gerasimov, E.S., Vattathil, S.M., Wynne, M.E., Liu, J., Lori, A., Faundez, V., Bennett, D.A., Seyfried, N.T., et al. (2022). Shared mechanisms across the major psychiatric and neurodegenerative diseases. Nat. Commun. *13*, 4314. https://doi.org/10.1038/s41467-022-31873-5.
8. Bellenguez, C., Küçükali, F., Jansen, I.E., Kleineidam, L., Moreno-Grau, S., Amin, N., Naj, A.C., Campos-Martin, R., Grenier-Boley, B., Andrade, V., et al. (2022). New insights into the genetic etiology of Alzheimer's disease and related dementias. Nat. Genet. *54*, 412–436. https://doi.org/10.1038/s41588-022-01024-z.
9. Scheltens, P., De Strooper, B., Kivipelto, M., Holstege, H., Chételat, G., Teunissen, C.E., Cummings, J., and van der Flier, W.M. (2021). Alzheimer's disease. Lancet *397*, 1577–1590. https://doi.org/10.1016/S0140-6736(20)32205-4.
10. Giri, M., Zhang, M., and Lü, Y. (2016). Genes associated with Alzheimer's disease: an overview and current status. Clin. Interv. Aging *11*, 665–681. https://doi.org/10.2147/CIA.S105769.
11. Sun, L., Zhou, R., Yang, G., and Shi, Y. (2017). Analysis of 138 pathogenic mutations in presenilin-1 on the in vitro production of Aβ42 and Aβ40 peptides by γ-secretase. Proc. Natl. Acad. Sci. USA *114*, E476–E485. https://doi.org/10.1073/pnas.1618657114.
12. Arboleda-Velasquez, J.F., Lopera, F., O'Hare, M., Delgado-Tirado, S., Marino, C., Chmielewska, N., Saez-Torres, K.L., Amarnani, D., Schultz, A.P., Sperling, R.A., et al. (2019). Resistance to autosomal dominant Alzheimer's disease in an APOE3 Christchurch homozygote: a case report. Nat. Med. *25*, 1680–1683. https://doi.org/10.1038/s41591-019-0611-3.
13. Chen, Y., Song, S., Parhizkar, S., Lord, J., Zhu, Y., Strickland, M.R., Wang, C., Park, J., Tabor, G.T., Jiang, H., et al. (2023). APOE3ch alters microglial response and suppresses Abeta-induced tau seeding and spread. Cell *187*, 428–445.e420. https://doi.org/10.1016/j.cell.2023.11.029.
14. Gomez Toledo, A., Sorrentino, J.T., Sandoval, D.R., Malmstrom, J., Lewis, N.E., and Esko, J.D. (2021). A Systems View of the Heparan Sulfate Interactome. J. Histochem. Cytochem. *69*, 105–119. https://doi.org/10.1369/0022155420988661.
15. Sarrazin, S., Lamanna, W.C., and Esko, J.D. (2011). Heparan sulfate proteoglycans. Cold Spring Harb. Perspect. Biol. *3*, a004952. https://doi.org/10.1101/cshperspect.a004952.
16. Schultheis, N., Becker, R., Berhanu, G., Kapral, A., Roseman, M., Shah, S., Connell, A., and Selleck, S. (2022). Regulation of autophagy, lipid metabolism, and neurodegenerative pathology by heparan sulfate proteoglycans. Front. Genet. *13*, 1012706. https://doi.org/10.3389/fgene.2022.1012706.
17. Dimou, E., Cosentino, K., Platonova, E., Ros, U., Sadeghi, M., Kashyap, P., Katsinelos, T., Wegehingel, S., Noé, F., García-Sáez, A.J., et al. (2019). Single event visualization of unconventional secretion of FGF2. J. Cell Biol. *218*, 683–699. https://doi.org/10.1083/jcb.201802008.
18. Merezhko, M., Brunello, C.A., Yan, X., Vihinen, H., Jokitalo, E., Uronen, R.L., and Huttunen, H.J. (2018). Secretion of Tau via an Unconventional Non-vesicular Mechanism. Cell Rep. *25*, 2027–2035.e4. https://doi.org/10.1016/j.celrep.2018.10.078.
19. Rushton, E., Kopke, D.L., and Broadie, K. (2020). Extracellular heparan sulfate proteoglycans and glycan-binding lectins orchestrate trans-synaptic signaling. J. Cell Sci. *133*, jcs244186. https://doi.org/10.1242/jcs.244186.
20. Reynolds-Peterson, C.E., Zhao, N., Xu, J., Serman, T.M., Xu, J., and Selleck, S.B. (2017). Heparan sulfate proteoglycans regulate autophagy in Drosophila. Autophagy *13*, 1262–1279. https://doi.org/10.1080/15548627.2017.1304867.
21. Reynolds-Peterson, C., Xu, J., Zhao, N., Cruse, C., Yonel, B., Trasorras, C., Toyoda, H., Kinoshita-Toyoda, A., Dobson, J., Schultheis, N., et al. (2020). Heparan Sulfate Structure Affects Autophagy, Lifespan, Responses to Oxidative Stress, and Cell Degeneration in Drosophila parkin Mutants. G3 (Bethesda) *10*, 129–141. https://doi.org/10.1534/g3.119.400730.
22. Checler, F., Goiran, T., and Alves da Costa, C. (2017). Presenilins at the crossroad of a functional interplay between PARK2/PARKIN and PINK1 to control mitophagy: Implication for neurodegenerative diseases. Autophagy *13*, 2004–2005. https://doi.org/10.1080/15548627.2017.1363950.
23. Costa-Laparra, I., Juárez-Escoto, E., Vicario, C., Moratalla, R., and García-Sanz, P. (2023). *APOE* ε4 allele, along with *G206D-PSEN1* mutation, alters mitochondrial networks and their degradation in Alzheimer's disease. Front. Aging Neurosci. *15*, 1087072. https://doi.org/10.3389/fnagi.2023.1087072.
24. Roca-Agujetas, V., de Dios, C., Abadin, X., and Colell, A. (2021). Upregulation of brain cholesterol levels inhibits mitophagy in Alzheimer disease. Autophagy *17*, 1555–1557. https://doi.org/10.1080/15548627.2021.1920814.
25. Rojas-Charry, L., Calero-Martinez, S., Morganti, C., Morciano, G., Park, K., Hagel, C., Marciniak, S.J., Glatzel, M., Pinton, P., and Sepulveda-Falla, D. (2020). Susceptibility to cellular stress in PS1 mutant N2a cells is associated with mitochondrial defects and altered calcium homeostasis. Sci. Rep. *10*, 6455. https://doi.org/10.1038/s41598-020-63254-7.
26. Schultheis, N., Jiang, M., and Selleck, S.B. (2021). Putting the brakes on autophagy: The role of heparan sulfate modified proteins in the balance of anabolic and catabolic pathways and intracellular quality control. Matrix Biol. *100–101*, 173–181. https://doi.org/10.1016/j.matbio.2021.01.006.
27. Anower-E-Khuda, F., Singh, G., Deng, Y., Gordts, P.L.S.M., and Esko, J.D. (2019). Triglyceride-rich lipoprotein binding and uptake by heparan sulfate proteoglycan receptors in a CRISPR/Cas9 library of Hep3B mutants. Glycobiology *29*, 582–592. https://doi.org/10.1093/glycob/cwz037.
28. Reitz, C., Jun, G., Naj, A., Rajbhandary, R., Vardarajan, B.N., Wang, L.S., Valladares, O., Lin, C.F., Larson, E.B., Graff-Radford, N.R., et al. (2013). Variants in the ATP-binding cassette transporter (ABCA7), apolipoprotein E 4,and the risk of late-onset Alzheimer disease in African Americans. JAMA, J. Am. Med. Assoc. *309*, 1483–1492. https://doi.org/10.1001/jama.2013.2973.
29. Hollingworth, P., Harold, D., Sims, R., Gerrish, A., Lambert, J.C., Carrasquillo, M.M., Abraham, R., Hamshere, M.L., Pahwa, J.S., Moskvina, V., et al. (2011). Common variants at ABCA7, MS4A6A/MS4A4E, EPHA1, CD33 and CD2AP are associated with Alzheimer's disease. Nat. Genet. *43*, 429–435. https://doi.org/10.1038/ng.803.
30. Cukier, H.N., Kunkle, B.W., Vardarajan, B.N., Rolati, S., Hamilton-Nelson, K.L., Kohli, M.A., Whitehead, P.L., Dombroski, B.A., Van Booven, D., Lang, R., et al. (2016). ABCA7 frameshift deletion associated with Alzheimer disease in African Americans. Neurol. Genet. *2*, e79. https://doi.org/10.1212/NXG.0000000000000079.
31. De Roeck, A., Van den Bossche, T., van der Zee, J., Verheijen, J., De Coster, W., Van Dongen, J., Dillen, L., Baradaran-Heravi, Y., Heeman, B., Sanchez-Valle, R., et al. (2017). Deleterious ABCA7 mutations and transcript rescue mechanisms in early onset Alzheimer's disease. Acta Neuropathol. *134*, 475–487. https://doi.org/10.1007/s00401-017-1714-x.
32. Berger, J.H., Charron, M.J., and Silver, D.L. (2012). Major facilitator superfamily domain-containing protein 2a (MFSD2A) has roles in body growth, motor function, and lipid metabolism. PLoS One *7*, e50629. https://doi.org/10.1371/journal.pone.0050629.
33. Dong, Y.T., Cao, K., Xiang, J., Qi, X.L., Xiao, Y., Yu, W.F., He, Y., Hong, W., and Guan, Z.Z. (2023). Resveratrol Attenuates the Disruption of Lipid Metabolism Observed in Amyloid Precursor Protein/Presenilin 1

Mouse Brains and Cultured Primary Neurons Exposed to Aβ. Neuroscience *521*, 134–147. https://doi.org/10.1016/j.neuroscience.2023.04.023.

34. Haney, M.S., Palovics, R., Munson, C.N., Long, C., Johansson, P.K., Yip, O., Dong, W., Rawat, E., West, E., Schlachetzki, J.C.M., et al. (2024). APOE4/4 is linked to damaging lipid droplets in Alzheimer's disease microglia. Nature *628*, 154–161. https://doi.org/10.1038/s41586-024-07185-7.
35. Lin, J., Handschin, C., and Spiegelman, B.M. (2005). Metabolic control through the PGC-1 family of transcription coactivators. Cell Metab. *1*, 361–370. https://doi.org/10.1016/j.cmet.2005.05.004.
36. Dominy, J.E., Jr., Lee, Y., Gerhart-Hines, Z., and Puigserver, P. (2010). Nutrient-dependent regulation of PGC-1alpha's acetylation state and metabolic function through the enzymatic activities of Sirt1/GCN5. Biochim. Biophys. Acta *1804*, 1676–1683. https://doi.org/10.1016/j.bbapap.2009.11.023.
37. Yu, S., and Reddy, J.K. (2007). Transcription coactivators for peroxisome proliferator-activated receptors. Biochim. Biophys. Acta *1771*, 936–951. https://doi.org/10.1016/j.bbalip.2007.01.008.
38. Lambert, J.C., Ramirez, A., Grenier-Boley, B., and Bellenguez, C. (2023). Step by step: towards a better understanding of the genetic architecture of Alzheimer's disease. Mol. Psychiatry *28*, 2716–2727. https://doi.org/10.1038/s41380-023-02076-1.
39. Bertram, L., Lill, C.M., and Tanzi, R.E. (2010). The genetics of Alzheimer disease: back to the future. Neuron *68*, 270–281. https://doi.org/10.1016/j.neuron.2010.10.013.
40. Sullivan, S.E., Liao, M., Smith, R.V., White, C., Lagomarsino, V.N., Xu, J., Taga, M., Bennett, D.A., De Jager, P.L., and Young-Pearse, T.L. (2019). Candidate-based screening via gene modulation in human neurons and astrocytes implicates FERMT2 in Aβ and TAU proteostasis. Hum. Mol. Genet. *28*, 718–735. https://doi.org/10.1093/hmg/ddy376.
41. Bhattacharyya, R., Teves, C.A.F., Long, A., Hofert, M., and Tanzi, R.E. (2022). The neuronal-specific isoform of BIN1 regulates β-secretase cleavage of APP and Aβ generation in a RIN3-dependent manner. Sci. Rep. *12*, 3486. https://doi.org/10.1038/s41598-022-07372-4.
42. Shen, R., Zhao, X., He, L., Ding, Y., Xu, W., Lin, S., Fang, S., Yang, W., Sung, K., Spencer, B., et al. (2020). Upregulation of RIN3 induces endosomal dysfunction in Alzheimer's disease. Transl. Neurodegener. *9*, 26. https://doi.org/10.1186/s40035-020-00206-1.
43. Ren, Y., Kirkpatrick, C.A., Rawson, J.M., Sun, M., and Selleck, S.B. (2009). Cell type-specific requirements for heparan sulfate biosynthesis at the Drosophila neuromuscular junction: effects on synapse function, membrane trafficking, and mitochondrial localization. J. Neurosci. *29*, 8539–8550.
44. Weiss, R.J., Spahn, P.N., Chiang, A.W.T., Liu, Q., Li, J., Hamill, K.M., Rother, S., Clausen, T.M., Hoeksema, M.A., Timm, B.M., et al. (2021). Genome-wide screens uncover KDM2B as a modifier of protein binding to heparan sulfate. Nat. Chem. Biol. *17*, 684–692. https://doi.org/10.1038/s41589-021-00776-9.
45. Qi, G., Mi, Y., Shi, X., Gu, H., Brinton, R.D., and Yin, F. (2021). ApoE4 Impairs Neuron-Astrocyte Coupling of Fatty Acid Metabolism. Cell Rep. *34*, 108572. https://doi.org/10.1016/j.celrep.2020.108572.
46. Elson-Schwab, L., Garner, O.B., Schuksz, M., Crawford, B.E., Esko, J.D., and Tor, Y. (2007). Guanidinylated neomycin delivers large, bioactive cargo into cells through a heparan sulfate-dependent pathway. J. Biol. Chem. *282*, 13585–13591. https://doi.org/10.1074/jbc.M700463200.
47. De Strooper, B. (2003). Aph-1, Pen-2, and Nicastrin with Presenilin generate an active gamma-Secretase complex. Neuron *38*, 9–12. https://doi.org/10.1016/s0896-6273(03)00205-8.
48. Herreman, A., Van Gassen, G., Bentahir, M., Nyabi, O., Craessaerts, K., Mueller, U., Annaert, W., and De Strooper, B. (2003). gamma-Secretase activity requires the presenilin-dependent trafficking of nicastrin through the Golgi apparatus but not its complex glycosylation. J. Cell Sci. *116*, 1127–1136. https://doi.org/10.1242/jcs.00292.
49. Kelleher, R.J., 3rd, and Shen, J. (2017). Presenilin-1 mutations and Alzheimer's disease. Proc. Natl. Acad. Sci. USA *114*, 629–631. https://doi.org/10.1073/pnas.1619574114.
50. Deaton, C.A., and Johnson, G.V.W. (2020). Presenilin 1 Regulates Membrane Homeostatic Pathways that are Dysregulated in Alzheimer's Disease. J. Alzheimers Dis. *77*, 961–977. https://doi.org/10.3233/JAD-200598.
51. Bolduc, D.M., Montagna, D.R., Gu, Y., Selkoe, D.J., and Wolfe, M.S. (2016). Nicastrin functions to sterically hinder gamma-secretase-substrate interactions driven by substrate transmembrane domain. Proc. Natl. Acad. Sci. USA *113*, E509–E518. https://doi.org/10.1073/pnas.1512952113.
52. Kang, J., Shin, S., Perrimon, N., and Shen, J. (2017). An Evolutionarily Conserved Role of Presenilin in Neuronal Protection in the Aging Drosophila Brain. Genetics *206*, 1479–1493. https://doi.org/10.1534/genetics.116.196881.
53. Sun, J., Xu, A.Q., Giraud, J., Poppinga, H., Riemensperger, T., Fiala, A., and Birman, S. (2018). Neural Control of Startle-Induced Locomotion by the Mushroom Bodies and Associated Neurons in Drosophila. Front. Syst. Neurosci. *12*, 6. https://doi.org/10.3389/fnsys.2018.00006.
54. Behnke, J.A., Ye, C., Moberg, K.H., and Zheng, J.Q. (2021). A protocol to detect neurodegeneration in Drosophila melanogaster whole-brain mounts using advanced microscopy. STAR Protoc. *2*, 100689. https://doi.org/10.1016/j.xpro.2021.100689.
55. Ye, Y., and Fortini, M.E. (1999). Apoptotic activities of wild-type and Alzheimer's disease-related mutant presenilins in Drosophila melanogaster. J. Cell Biol. *146*, 1351–1364.
56. Gomez-Sequeda, N., Mendivil-Perez, M., Jimenez-Del-Rio, M., Lopera, F., and Velez-Pardo, C. (2023). Cholinergic-like neurons and cerebral spheroids bearing the PSEN1 p.Ile416Thr variant mirror Alzheimer's disease neuropathology. Sci. Rep. *13*, 12833. https://doi.org/10.1038/s41598-023-39630-4.
57. Mendivil-Perez, M., Velez-Pardo, C., Lopera, F., Kosik, K.S., and Jimenez-Del-Rio, M. (2023). PSEN1 E280A Cholinergic-like Neurons and Cerebral Spheroids Derived from Mesenchymal Stromal Cells and from Induced Pluripotent Stem Cells Are Neuropathologically Equivalent. Int. J. Mol. Sci. *24*, 8957. https://doi.org/10.3390/ijms24108957.
58. Denton, D., and Kumar, S. (2015). Using the vital dye acridine orange to detect dying cells in Drosophila. Cold Spring Harb. Protoc. *2015*, 572–575. https://doi.org/10.1101/pdb.prot086207.
59. Atale, N., Gupta, S., Yadav, U.C.S., and Rani, V. (2014). Cell-death assessment by fluorescent and nonfluorescent cytosolic and nuclear staining techniques. J. Microsc. *255*, 7–19. https://doi.org/10.1111/jmi.12133.
60. Chan, R.B., Oliveira, T.G., Cortes, E.P., Honig, L.S., Duff, K.E., Small, S.A., Wenk, M.R., Shui, G., and Di Paolo, G. (2012). Comparative lipidomic analysis of mouse and human brain with Alzheimer disease. J. Biol. Chem. *287*, 2678–2688. https://doi.org/10.1074/jbc.M111.274142.
61. Demir, E., and Kacew, S. (2023). Drosophila as a Robust Model System for Assessing Autophagy: A Review. Toxics *11*, 682. https://doi.org/10.3390/toxics11080682.
62. Partridge, L., Alic, N., Bjedov, I., and Piper, M.D.W. (2011). Ageing in Drosophila: the role of the insulin/Igf and TOR signalling network. Exp. Gerontol. *46*, 376–381. https://doi.org/10.1016/j.exger.2010.09.003.
63. Zhou, J., Xu, L., Duan, X., Liu, W., Zhao, X., Wang, X., Shang, W., Fang, X., Yang, H., Jia, L., et al. (2019). Large-scale RNAi screen identified Dhpr as a regulator of mitochondrial morphology and tissue homeostasis. Sci. Adv. *5*, eaax0365. https://doi.org/10.1126/sciadv.aax0365.
64. Rusten, T.E., Lindmo, K., Juhász, G., Sass, M., Seglen, P.O., Brech, A., and Stenmark, H. (2004). Programmed autophagy in the Drosophila fat body is induced by ecdysone through regulation of the PI3K pathway. Dev. Cell *7*, 179–192. https://doi.org/10.1016/j.devcel.2004.07.005.
65. Rambold, A.S., Cohen, S., and Lippincott-Schwartz, J. (2015). Fatty acid trafficking in starved cells: regulation by lipid droplet lipolysis, autophagy, and mitochondrial fusion dynamics. Dev. Cell *32*, 678–692. https://doi.org/10.1016/j.devcel.2015.01.029.
66. Xu, D., Vincent, A., González-Gutiérrez, A., Aleyakpo, B., Anoar, S., Giblin, A., Atilano, M.L., Adams, M., Shen, D., Thoeng, A., et al. (2023). A monocarboxylate transporter rescues frontotemporal dementia and Alzheimer's disease models. PLoS Genet. *19*, e1010893. https://doi.org/10.1371/journal.pgen.1010893.
67. Yildirim, K., Winkler, B., Pogodalla, N., Mackensen, S., Baldenius, M., Garcia, L., Naffin, E., Rodrigues, S., and Klämbt, C. (2022). Redundant functions of the SLC5A transporters Rumpel, Bumpel, and Kumpel in ensheathing glial cells. Biol. Open *11*, bio059128. https://doi.org/10.1242/bio.059128.
68. Khries, M., Lim, A., Mitra, D., Anderson, M., Bengtsson, J., Bowron, A., Harris, E., Blickwedel, J., Wood, K., and Basu, A.P. (2023). Broadening the Spectrum of SLC22A5 Phenotype: Primary Carnitine

Deficiency Presenting with Focal Myoclonus. Child Neurol. Open *10*, 2329048X231184183. https://doi.org/10.1177/2329048X231184183.

69. Koleske, M.L., McInnes, G., Brown, J.E.H., Thomas, N., Hutchinson, K., Chin, M.Y., Koehl, A., Arkin, M.R., Schlessinger, A., Gallagher, R.C., et al. (2022). Functional genomics of OCTN2 variants informs protein-specific variant effect predictor for Carnitine Transporter Deficiency. Proc. Natl. Acad. Sci. USA *119*, e2210247119. https://doi.org/10.1073/pnas.2210247119.
70. Lang, S., Hilsabeck, T.A., Wilson, K.A., Sharma, A., Bose, N., Brackman, D.J., Beck, J.N., Chen, L., Watson, M.A., Killilea, D.W., et al. (2019). A conserved role of the insulin-like signaling pathway in diet-dependent uric acid pathologies in Drosophila melanogaster. PLoS Genet. *15*, e1008318. https://doi.org/10.1371/journal.pgen.1008318.
71. Rommelaere, S., Boquete, J.P., Piton, J., Kondo, S., and Lemaitre, B. (2019). The Exchangeable Apolipoprotein Nplp2 Sustains Lipid Flow and Heat Acclimation in Drosophila. Cell Rep. *27*, 886–899.e6. https://doi.org/10.1016/j.celrep.2019.03.074.
72. Ratnaparkhi, A., and Sudhakaran, J. (2022). Neural pathways in nutrient sensing and insulin signaling. Front. Physiol. *13*, 1002183. https://doi.org/10.3389/fphys.2022.1002183.
73. Xu, T., Nicolson, S., Sandow, J.J., Dayan, S., Jiang, X., Manning, J.A., Webb, A.I., Kumar, S., and Denton, D. (2021). Cp1/cathepsin L is required for autolysosomal clearance in Drosophila. Autophagy *17*, 2734–2749. https://doi.org/10.1080/15548627.2020.1838105.
74. Qian, W., Guo, M., Peng, J., Zhao, T., Li, Z., Yang, Y., Li, H., Zhang, X., King-Jones, K., and Cheng, D. (2023). Decapentaplegic retards lipolysis during metamorphosis in Bombyx mori and Drosophila melanogaster. Insect Biochem. Mol. Biol. *155*, 103928. https://doi.org/10.1016/j.ibmb.2023.103928.
75. Jackson, S.M., Nakato, H., Sugiura, M., Jannuzi, A., Oakes, R., Kaluza, V., Golden, C., and Selleck, S.B. (1997). dally, a Drosophila glypican, controls cellular responses to the TGF-beta-related morphogen, Dpp. Dpp. Development *124*, 4113–4120.
76. Nybakken, K., and Perrimon, N. (2002). Heparan sulfate proteoglycan modulation of developmental signaling in Drosophila. Biochim. Biophys. Acta *1573*, 280–291.
77. Snow, A.D., Cummings, J.A., and Lake, T. (2021). The Unifying Hypothesis of Alzheimer's Disease: Heparan Sulfate Proteoglycans/Glycosaminoglycans Are Key as First Hypothesized Over 30 Years Ago. Front. Aging Neurosci. *13*, 710683. https://doi.org/10.3389/fnagi.2021.710683.
78. Ning, L., Xu, Z., Furuya, N., Nonaka, R., Yamada, Y., and Arikawa-Hirasawa, E. (2015). Perlecan inhibits autophagy to maintain muscle homeostasis in mouse soleus muscle. Matrix Biol. *48*, 26–35. https://doi.org/10.1016/j.matbio.2015.08.002.
79. Yamashita, Y., Nakada, S., Yoshihara, T., Nara, T., Furuya, N., Miida, T., Hattori, N., and Arikawa-Hirasawa, E. (2018). Perlecan, a heparan sulfate proteoglycan, regulates systemic metabolism with dynamic changes in adipose tissue and skeletal muscle. Sci. Rep. *8*, 7766. https://doi.org/10.1038/s41598-018-25635-x.
80. Bao, L., Chandra, P.K., Moroz, K., Zhang, X., Thung, S.N., Wu, T., and Dash, S. (2014). Impaired autophagy response in human hepatocellular carcinoma. Exp. Mol. Pathol. *96*, 149–154. https://doi.org/10.1016/j.yexmp.2013.12.002.
81. Hu, P., Cheng, B., He, Y., Wei, Z., Wu, D., and Meng, Z. (2018). Autophagy suppresses proliferation of HepG2 cells via inhibiting glypican-3/wnt/β-catenin signaling. OncoTargets Ther. *11*, 193–200. https://doi.org/10.2147/OTT.S150520.
82. Hu, P., Ke, C., Guo, X., Ren, P., Tong, Y., Luo, S., He, Y., Wei, Z., Cheng, B., Li, R., et al. (2019). Both glypican-3/Wnt/β-catenin signaling pathway and autophagy contributed to the inhibitory effect of curcumin on hepatocellular carcinoma. Dig. Liver Dis. *51*, 120–126. https://doi.org/10.1016/j.dld.2018.06.012.
83. Chong, C.M., Ke, M., Tan, Y., Huang, Z., Zhang, K., Ai, N., Ge, W., Qin, D., Lu, J.H., and Su, H. (2018). Presenilin 1 deficiency suppresses autophagy in human neural stem cells through reducing gamma-secretase-independent ERK/CREB signaling. Cell Death Dis. *9*, 879. https://doi.org/10.1038/s41419-018-0945-7.
84. Lee, J.H., Yu, W.H., Kumar, A., Lee, S., Mohan, P.S., Peterhoff, C.M., Wolfe, D.M., Martinez-Vicente, M., Massey, A.C., Sovak, G., et al. (2010). Lysosomal proteolysis and autophagy require presenilin 1 and are disrupted by Alzheimer-related PS1 mutations. Cell *141*, 1146–1158. https://doi.org/10.1016/j.cell.2010.05.008.
85. Li, L., Roh, J.H., Chang, E.H., Lee, Y., Lee, S., Kim, M., Koh, W., Chang, J.W., Kim, H.J., Nakanishi, M., et al. (2018). iPSC Modeling of Presenilin1 Mutation in Alzheimer's Disease with Cerebellar Ataxia. Exp. Neurobiol. *27*, 350–364. https://doi.org/10.5607/en.2018.27.5.350.
86. Ryan, K.C., Ashkavand, Z., Sarasija, S., Laboy, J.T., Samarakoon, R., and Norman, K.R. (2021). Increased mitochondrial calcium uptake and concomitant mitochondrial activity by presenilin loss promotes mTORC1 signaling to drive neurodegeneration. Aging Cell *20*, e13472. https://doi.org/10.1111/acel.13472.
87. Martin-Maestro, P., Sproul, A., Martinez, H., Paquet, D., Gerges, M., Noggle, S., and Starkov, A.A. (2019). Autophagy Induction by Bexarotene Promotes Mitophagy in Presenilin 1 Familial Alzheimer's Disease iPSC-Derived Neural Stem Cells. Mol. Neurobiol. *56*, 8220–8236. https://doi.org/10.1007/s12035-019-01665-y.
88. Mizielinska, S., Grönke, S., Niccoli, T., Ridler, C.E., Clayton, E.L., Devoy, A., Moens, T., Norona, F.E., Woollacott, I.O.C., Pietrzyk, J., et al. (2014). C9orf72 repeat expansions cause neurodegeneration in Drosophila through arginine-rich proteins. Science *345*, 1192–1194. https://doi.org/10.1126/science.1256800.
89. Liu, L., MacKenzie, K.R., Putluri, N., Maletić-Savatić, M., and Bellen, H.J. (2017). The Glia-Neuron Lactate Shuttle and Elevated ROS Promote Lipid Synthesis in Neurons and Lipid Droplet Accumulation in Glia via APOE/D. Cell Metab. *26*, 719–737.e6. https://doi.org/10.1016/j.cmet.2017.08.024.
90. Toyoda, H., Kinoshita-Toyoda, A., Fox, B., and Selleck, S.B. (2000). Structural analysis of glycosaminoglycans in animals bearing mutations in sugarless, sulfateless, and tout-velu. Drosophila homologues of vertebrate genes encoding glycosaminoglycan biosynthetic enzymes. J. Biol. Chem. *275*, 21856–21861. https://doi.org/10.1074/jbc.M003540200.
91. Toyoda, H., Kinoshita-Toyoda, A., and Selleck, S.B. (2000). Structural analysis of glycosaminoglycans in Drosophila and Caenorhabditis elegans and demonstration that tout-velu, a Drosophila gene related to EXT tumor suppressors, affects heparan sulfate in vivo. J. Biol. Chem. *275*, 2269–2275.
92. Nakato, E., Baker, S., Kinoshita-Toyoda, A., Knudsen, C., Lu, Y.S., Takemura, M., Toyoda, H., and Nakato, H. (2024). In vivo activities of heparan sulfate differentially modified by NDSTs during development. Proteoglycan Res. *2*, e17. https://doi.org/10.1002/pgr2.17.
93. Holmes, B.B., DeVos, S.L., Kfoury, N., Li, M., Jacks, R., Yanamandra, K., Ouidja, M.O., Brodsky, F.M., Marasa, J., Bagchi, D.P., et al. (2013). Heparan sulfate proteoglycans mediate internalization and propagation of specific proteopathic seeds. Proc. Natl. Acad. Sci. USA *110*, E3138–E3147. https://doi.org/10.1073/pnas.1301440110.
94. Stopschinski, B.E., Holmes, B.B., Miller, G.M., Manon, V.A., Vaquer-Alicea, J., Prueitt, W.L., Hsieh-Wilson, L.C., and Diamond, M.I. (2018). Specific glycosaminoglycan chain length and sulfation patterns are required for cell uptake of tau versus alpha-synuclein and beta-amyloid aggregates. J. Biol. Chem. *293*, 10826–10840. https://doi.org/10.1074/jbc.RA117.000378.
95. Wang, Z., Patel, V.N., Song, X., Xu, Y., Kaminski, A.M., Doan, V.U., Su, G., Liao, Y., Mah, D., Zhang, F., et al. (2023). Increased 3-O-sulfated heparan sulfate in Alzheimer's disease brain is associated with genetic risk gene HS3ST1. Sci. Adv. *9*, eadf6232. https://doi.org/10.1126/sciadv.adf6232.
96. Ferreira, A., Royaux, I., Liu, J., Wang, Z., Su, G., Moechars, D., Callewaert, N., and De Muynck, L. (2022). The 3-O sulfation of heparan sulfate proteoglycans contributes to the cellular internalization of tau aggregates. BMC Mol. Cell Biol. *23*, 61. https://doi.org/10.1186/s12860-022-00462-1.
97. Witoelar, A., Rongve, A., Almdahl, I.S., Ulstein, I.D., Engvig, A., White, L.R., Selbæk, G., Stordal, E., Andersen, F., Brækhus, A., et al. (2018). Meta-analysis of Alzheimer's disease on 9,751 samples from Norway and IGAP study identifies four risk loci. Sci. Rep. *8*, 18088. https://doi.org/10.1038/s41598-018-36429-6.
98. Thacker, B.E., Xu, D., Lawrence, R., and Esko, J.D. (2014). Heparan sulfate 3-O-sulfation: a rare modification in search of a function. Matrix Biol. *35*, 60–72. https://doi.org/10.1016/j.matbio.2013.12.001.
99. Jendresen, C.B., Cui, H., Zhang, X., Vlodavsky, I., Nilsson, L.N.G., and Li, J.P. (2015). Overexpression of heparanase lowers the amyloid burden in amyloid-beta precursor protein transgenic mice. J. Biol. Chem. *290*, 5053–5064. https://doi.org/10.1074/jbc.M114.600569.
100. Liu, C.C., Zhao, N., Yamaguchi, Y., Cirrito, J.R., Kanekiyo, T., Holtzman, D.M., and Bu,

G. (2016). Neuronal heparan sulfates promote amyloid pathology by modulating brain amyloid-beta clearance and aggregation in Alzheimer's disease. Sci. Transl. Med. *8*, 332ra44. https://doi.org/10.1126/scitranslmed.aad3650.

101. Huang, Y., and Mahley, R.W. (2014). Apolipoprotein E: structure and function in lipid metabolism, neurobiology, and Alzheimer's diseases. Neurobiol Dis *72 Pt*. Neurobiol. Dis. *72 Pt A*, 3–12. https://doi.org/10.1016/j.nbd.2014.08.025.
102. Watts, J.A., Grunseich, C., Rodriguez, Y., Liu, Y., Li, D., Burdick, J.T., Bruzel, A., Crouch, R.J., Mahley, R.W., Wilson, S.H., and Cheung, V.G. (2022). A common transcriptional mechanism involving R-loop and RNA abasic site regulates an enhancer RNA of APOE. Nucleic Acids Res. *50*, 12497–12514. https://doi.org/10.1093/nar/gkac1107.
103. Campos-Pena, V., Pichardo-Rojas, P., Sanchez-Barbosa, T., Ortiz-Islas, E., Rodriguez-Perez, C.E., Montes, P., Ramos-Palacios, G., Silva-Adaya, D., Valencia-Quintana, R., Cerna-Cortes, J.F., and Toral-Rios, D. (2022). Amyloid beta, Lipid Metabolism, Basal Cholinergic System, and Therapeutics in Alzheimer's Disease. Int. J. Mol. Sci. *23*, 12092. https://doi.org/10.3390/ijms232012092.
104. Lam, V., Takechi, R., Hackett, M.J., Francis, R., Bynevelt, M., Celliers, L.M., Nesbit, M., Mamsa, S., Arfuso, F., Das, S., et al. (2021). Synthesis of human amyloid restricted to liver results in an Alzheimer disease-like neurodegenerative phenotype. PLoS Biol. *19*, e3001358. https://doi.org/10.1371/journal.pbio.3001358.
105. Juhasz, G., Hill, J.H., Yan, Y., Sass, M., Baehrecke, E.H., Backer, J.M., and Neufeld, T.P. (2008). The class III PI(3)K Vps34 promotes autophagy and endocytosis but not TOR signaling in Drosophila. J. Cell Biol. *181*, 655–666. https://doi.org/10.1083/jcb.200712051.
106. Sarbassov, D.D., Guertin, D.A., Ali, S.M., and Sabatini, D.M. (2005). Phosphorylation and regulation of Akt/PKB by the rictor-mTOR complex. Science *307*, 1098–1101.
107. Schindelin, J., Arganda-Carreras, I., Frise, E., Kaynig, V., Longair, M., Pietzsch, T., Preibisch, S., Rueden, C., Saalfeld, S., Schmid, B., et al. (2012). Fiji: an open-source platform for biological-image analysis. Nat. Methods *9*, 676–682. https://doi.org/10.1038/nmeth.2019.
108. Mitchell, K.J., and Staveley, B.E. (2006). Protocol for the detection and analysis of cell death in the adult Drosophila brain. Drosoph. Inf. Serv. *89*, 118–121.
109. Chen, E.Y., Tan, C.M., Kou, Y., Duan, Q., Wang, Z., Meirelles, G.V., Clark, N.R., and Ma'ayan, A. (2013). Enrichr: interactive and collaborative HTML5 gene list enrichment analysis tool. BMC Bioinf. *14*, 128. https://doi.org/10.1186/1471-2105-14-128.
110. Kuleshov, M.V., Jones, M.R., Rouillard, A.D., Fernandez, N.F., Duan, Q., Wang, Z., Koplev, S., Jenkins, S.L., Jagodnik, K.M., Lachmann, A., et al. (2016). Enrichr: a comprehensive gene set enrichment analysis web server 2016 update. Nucleic Acids Res. *44*, W90–W97. https://doi.org/10.1093/nar/gkw377.

STAR★METHODS

KEY RESOURCES TABLE

REAGENT or RESOURCE	SOURCE	IDENTIFIER
Bacterial and virus strains		
Lentivirus Negative Scramble shRNA Target Sequence: GCACTACCAGAGCTAACTCAGATAGTACT	Origene	Cat#TR30021
Lentivirus *NDST1* KD Target Sequence: TTCCACAACCAATCTGTGCTGGCAGAGCA	Origene	Cat#TL509817A
Chemicals, peptides, and recombinant proteins		
Alexa Fluor™ 594 Phalloidin	Thermofisher	Cat#A12381
MitoTracker™ Red CMXRos	Thermofisher	Cat#M7512
HCS LipidTOX™ Red Neutral Lipid Stain	Thermofisher	Cat#H34476
HCS LipidTOX™ Green Neutral Lipid Stain	Thermofisher	Cat#H34475
Biotracker MitoBlue Live Cell Dye	Sigma-Aldrich	Cat#SCT086
Prolong™ Gold Antifade Mountant with DAPI	Thermofisher	Cat#P36941
Vectashield Antifade Mounting Medium	Fisher Scientific	Cat#NC9532821
GNeo-biotin	Synthesized as described[44]	N/A
Hoescht 33342 Solution	Thermofisher	Cat#62249
Rapamycin	ApexBio	Cat#A8167
Acridine Orange	Thermofisher	Cat#A1301
Critical commercial assays		
Macherey-Nagel NucleoSpin® RNA Kit	VWR	Cat#MANA740955.50
Adult Brain Dissociation Kit	Miltenyi Biotech	Cat#130-107-677
Deposited data		
FASTQ of *Drosophila melanogaster* RNAseq Data	NCBI SRA Database	Accession# PRJNA1106548
FASTQ of Hep3B cells RNAseq Data	NCBI SRA Database	Accession# PRJNA1107266
Experimental models: Cell lines		
Human: A375 Cells: Wildtype	Gift from J. Esko, UCSD	N/A
Human: A375 Cells: *NDST1* KO	Gift from J. Esko, UCSD	N/A
Human: HEK293T Cells: Scramble	This paper: transfected by Anoop Narayanan	N/A
Human: HEK293T Cells: *NDST1* KD	This paper: transfected by Anoop Narayanan	N/A
Human: HEK293T Cells: *EXT1* KD	This paper: transfected by Anoop Narayanan	N/A
Human: Hep3B Cells: Wildtype	Gift from J. Esko, UCSD[27]	N/A
Human: Hep3B Cells: *EXT1* KO	Gift from J. Esko, UCSD[27]	N/A
Experimental models: Organisms/strains		
D. melanogaster: *UAS-shPsn2*	Gift from J. Kang, Harvard University[52]	N/A
D. melanogaster: *UAS-shPsn3*	Gift from J. Kang, Harvard University	N/A
D. melanogaster: *UAS-Nct^{RNAi}*	Gift from J. Kang, Harvard University	N/A
D. melanogaster: *c*155 elav-gal4; UAS-DcrII*	Bloomington Drosophila Stock Center (NIH P40OD018537)	RRID: BDSC 25750
D. melanogaster: *UAS-GFP-Atg8a*	Gift from T. Neufeld, University of Minnesota, Minneapolis, MN[105]	N/A
D. melanogaster: *UAS-w^{RNAi}*	Vienna Drosophila Resource Center (VDRC, www.vdrc.at).	RRID: BDSC 30033

(*Continued on next page*)

Continued

REAGENT or RESOURCE	SOURCE	IDENTIFIER
D. melanogaster: *R4-Gal4*	Bloomington Drosophila Stock Center (NIH P40OD018537)	RRID: BDSC 33832
D. melanogaster: *sfl*^{03844}	Bloomington Drosophila Stock Center (NIH P40OD018537)	RRID: BDSC 5575
D. melanogaster: *UAS-sfl*^{RNAi}	Bloomington Drosophila Stock Center (NIH P40OD018537)	RRID: BDSC 34601
D. melanogaster: *UAS-GFP-Atg8a; R4-Gal4*	Made in-lab[20]	N/A
D. melanogaster: *shPsn3; sfl*^{03844}	This manuscript	N/A
D. melanogaster: *shPsn3; UAS-sfl*^{RNAi}	This manuscript	N/A
Mouse: humanized *ApoE3* astrocytes	Obtained as described.[45]	N/A
Mouse: humanized *ApoE4* astrocytes	Obtained as described.[45]	N/A
Recombinant DNA		
Scramble shRNA Hairpin Sequence: CCTAAGGTTAAGTCGCCCTCGCTC GAGCGAGGGCGACTTAACCTTAGG	Sarbassov et al.[106]	RRID: Addgene 1864
NDST1 shRNA Target Sequence: TCTCGGCCTACTACCTATATG	Sigma-Aldrich	Cat#TRCN0000232002
EXT1 shRNA Target Sequence: CCCAACTTTGATGTTTCTATT	Sigma-Aldrich	Cat#TRCN0000039995
Software and algorithms		
ImageJ Fiji	Described in Schindelin et al.[107]	https://imagej.net/software/fiji/downloads
MiniTab	MiniTab	N/A
Psomagen mRNA Sequencing	Psomagen	N/A
BasePair RNA Seq Analysis	BasePair	N/A
GraphPad Prism v10.0		
FlowJo Analytical Software v10.8.0	FlowJo	N/A
Avizo	Thermofisher	N/A
Imaris 9.3.0	Oxford Instruments	N/A

RESOURCE AVAILABILITY

Lead contact

Further information and requests for resources should be directed to and will be fulfilled by the Lead Contact, Scott Selleck (sbs24@psu.edu).

Materials availability

Fly and cell lines used in this study are available upon request.

Data and code availability

- Data: Raw RNAseq data (FASTQ) of *Drosophila melanogaster* fat body have been deposited in NCBI Sequence Read Archive (SRA): https://www.ncbi.nlm.nih.gov/sra/PRJNA1106548, with data identification number PRJNA1106548. Raw RNAseq data (FASTQ) of Hep3B cells RNAseq have been deposited in NCBI Sequence Read Archive (SRA): https://www.ncbi.nlm.nih.gov/sra/PRJNA1107266, with data identification number PRJNA1107266. Differential Gene Expression Data from this study are provided in Tables S7 and S8.
- Code: This paper does not report any original code.
- Additional Information: Any additional information required to reanalyze the data reported in this paper is available from the lead contact upon request.

EXPERIMENTAL MODEL AND STUDY PARTICIPANT DETAILS

Mouse

All animal experiments were approved by the University of Arizona Institutional Animal Care and Use Committee (IACUC). Humanized ApoE3 (029018) and ApoE4 (027894) knockin mice (homozygous) and the wild-type C57BL/6J mice were obtained from the Jackson Laboratory and bred at the University of Arizona animal facility. All mice were housed in a temperature (23C) and humidity-controlled room with a 12-h light and 12-h dark cycle with *ad libitum* access to water and standard laboratory global 2019 diet (23% calories from protein, 22% calories from fat, 55% calories from carbohydrate, 3.3 kcal/g; Envigo) and cared in facilities operated by University Animal Care. 3-month male mice were used for primary astrocyte isolation and *in vivo*/*ex vivo* assays. Timed pregnant mice of designated genotype were prepared for the isolation of E17 embryonic hippocampal neurons.

Drosophila melanogaster

Fly strains were raised on standard cornmeal/sucrose/agar media at 25°C under a 12 h day/12 h night cycle. w^{1118} served as the wild-type stock. [UAS-*Atg8a* RNAi (43097)] and [UAS-*w* RNAi (30033)] RNAi strains were obtained from the Vienna *Drosophila* Resource Center (VDRC). [UAS-*sfl* RNAi (34601)], [sfl^{03844} (5575)], and [c*155 elav-gal4; UAS-dcrII (25750)] were obtained from the Bloomington *Drosophila* Stock Center (BDSC). [UAS-shPsn2] and [UAS shPsn3] flies were a generous gift from J. Shen and Norbert Perrimon, Harvard Medical School, Boston, MA. [shPsn3; UAS-*sfl* RNAi] and [shPsn3RNAi; sfl^{03844}] stocks were generated in lab. Where sex, developmental stage, and age is an influence it is noted in the results.

Human cell lines

A375, Hep3B, and HEK293T cell lines were cultured in DMEM supplemented with 10% fetal bovine serum (FBS) and 1% penicillin/streptomycin at 37°C, 5% CO_2 (Gibco). All human cell lines were tested for mycoplasma at initiation of all experiments. A375 cells were first isolated from a 54-year old female. Hep3B cells were first isolated from an 8-year old black male. HEK293T cells were first isolated from a female fetus.

METHOD DETAILS

Drosophila brain dissection and assessment of neurodegeneration

Following eclosion, flies were sorted by sex and aged for 7 or 30 days. Whole flies were fixed in 4% PFA containing 0.5% Triton X-100 (0.5% PBS-T) for 3h with nutation at 20°C. The samples were washed 4 times with 0.5% PBS-T for 15 min with nutation at 20°C. Brains were dissected from whole flies in 0.008% PBS-T and placed in staining solution (DAPI at 1:1000 and Phalloidin at 1:100 in 0.5% PBS-T) for 16-24h with nutation at 4°C. Following staining, brains were washed 4 times with 0.5% PBS-T for 15 min with nutation at 20°C and once with 1xPBS for 30 min with nutation at 20°C to remove any residual detergent or stain. A SecureSeal imaging spacer was applied to each microscope slide, and brains were mounted anterior side up with SlowFade Gold Antifade Mountant (without DAPI). A more detailed version of this procedure can be found in.[54] Full brain samples were imaged non-sequentially on an Olympus FV3000 confocal microscope at a step size of 2 μm. Images were analyzed in Fiji ImageJ using the trace and measure tools. The Look Up table was set to Fire, and the maximum pixel intensity was adjusted to provide optimal visualization of vacuoles. Once a vacuole could be distinguished from a tracheole, it was traced in the slice in which the diameter was the largest. The total number of vacuoles per brain and the total area of vacuoles per brain were summed, respectively. ANOVA statistical analysis (one-way, Tukey comparison) was performed in Minitab to confirm significance.

Acridine orange brain staining of *Drosophila* adult brain[108]

Following eclosion, flies were sorted by sex and aged 1 to 3 weeks. Female flies were knocked out with CO_2 and placed in 70% ethanol for 1 min before being transferred to a dissection tray containing Ringer's solution. After dissection, the brains were stained with 30 μL of 5 μg/mL Acridine Orange for 5 min on a glass microscope slide. The staining solution was removed, the brains were washed 1 time with 50 μL of Ringer's solution, and 50 μL of fresh Ringer's solution was added as a mounting medium. Full brain samples were imaged on an Olympus FV3000 confocal microscope at a step size of 2 μm. Images were analyzed in Fiji ImageJ as z stack maximum intensity projections. The Freehand Select tool was used to trace the outline of the most anatomically complete lobe and the area of this selection was measured. The image threshold was adjusted to remove background signal and the area outside the outlined tracing was deleted. The resulting image was converted into a binary pixel scheme, and the number of white pixels was measured. This value was normalized by the area of the tracing, and an average number of pixels per area per genotype was calculated.

Negative geotaxis assay

The behavioral abilities of Drosophila were measured via a startle-induced negative geotaxis protocol.[53] Upon eclosion, flies were separated by sex and aged for 3–6 days. For each geotaxis assay, 10 flies were placed into the apparatus and a startle response was induced by firmly tapping the apparatus on a mat until all flies had fallen to the bottom. The number of flies above the 8 cm line after 10 s was recorded and the flies were given a 60-s rest period before the next trial was performed. An average of 5 repetitions per vial of flies was taken as a single data point.

MitoTracker red staining of fat body

The fat body of third instar *Drosophila melanogaster* larvae were dissected in PBS and transferred to a 100 nM solution of MitoTracker Red CMXROS. They were incubated at room temperature for 30 min out of light. The fat bodies were washed in PBS and then fixed in a 4% v/v PFA solution where they were incubated at room temperature for 30 min out of light. After fixation, the fat body was washed in PBS and transferred to the glass imaging slide. ProLong Gold Antifade Mountant with DNA Stain DAPI was applied to the fat bodies as a mounting medium with counterstain. The fat bodies were imaged with an Olympus FV3000 confocal microscope.

Images of fat body stained with MitoTracker Red CMXRos were processed in Fiji ImageJ on a maximum intensity projection. An auto-threshold was applied to the images through Max Entropy. A watershed was applied and segmented mitochondria. Particles were selected for those between 1 and 10 μm in area and between 0.25 and 1.00 in circularity.

The size of mitochondria was analyzed using the built-in particle analysis tool in Fiji ImageJ on a maximum intensity projection. A 200×200 pixel box was used as a sample area, with the upper left pixel being the locator pixel that corresponded to the coordinates of the box. A random number generator was used to select two numbers between 0 and 824 to generate a random (x,y) coordinate to place the box. If the box was not entirely over a region where signal was present, the coordinates were reselected. Each sample was analyzed using this method three times, ensuring that the analyzed areas did not overlap.

LipidTox red staining of fat body

The fat body of third instar *Drosophila melanogaster* larvae were dissected in PBS and then fixed in a 4% v/v PFA solution where they were incubated at room temperature for 30 min out of light. After fixation, the fat bodies were washed in PBS. Fat bodies were then transferred to a LipidTox Red solution diluted 1:999 in buffer and incubated for 30 min at room temperature out of light. After staining, the fat bodies were transferred to a glass imaging slide. ProLong Gold Antifade Mountant with DNA Stain DAPI was applied to the fat bodies as a mounting medium with counterstain. The fat body tissue was imaged with an Olympus FV3000 confocal microscope.

Transmission electron microscopy

Fat body tissues were dissected out of third-instar larvae and stored overnight in a refrigerator in Modified Karnovsky's fixative. Samples were washed three times in 0.1M cacodylate buffer and subsequently fixed for 1 h in 1–2% Osmium tetroxide in 0.1M cacodylate buffer. Samples were washed two times with 0.1M cacodylate buffer and one time with milliQ water before undergoing an *en bloc* stain for 1 h in filtered 2% aqueous Uranyl acetate. Samples were dehydrated in progressively increasing ethanol concentrations (50%, 70%, 85%, 90%, 100%, 3xEM grade ethanol) followed by three acetone dehydrations. Samples were infiltrated with Spurr's resin and imaged.

Samples were examined using FEI Tecnai G2 Spirit BioTwin and FEI Talos 200C microscopes.

RNA isolation

RNA was isolated according to the Macherey-Nagel NucleoSpin RNA Kit protocol for cultured cells and tissue. Briefly, Hep3B or *Drosophila melanogaster* fatbody cells were lysed in 350 μL Buffer RA1 and 3.5 μL β-mercaptoethanol and then filtered through a NucleoSpin Filter column through centrifugation for 1 min at 11,000 × *g*. The lysate was then mixed with 350 μL 70% ethanol and passed through a NucleoSpin RNA Column at 11,000 × *g* for 30 s in order to bind the RNA to the column. The binding step was repeated three additional times for lysate from fatbody. 350 μL of Membrane Desalting Buffer was added to the NucleoSpin RNA Column and centrifuged for 1 min at 11,000 × *g*. 95 μL of a DNase reaction mixture was incubated on the column for 15 min at room temperature to digest DNA. After digestion, 200 μL of Buffer RAW2 was applied to the column and centrifuged for 30 s at 11,000 × *g* to inactivate the rDNase. 600 μL of Buffer RA3 was then added to the column and centrifuged for 30 s at 11,000 × *g*. 250 μL of Buffer RA3 was applied to the column and centrifuged for 2 min at 11,000 × *g* to dry the membrane. 60 μL of RNase-free H_2O was applied to the column and centrifuged at 11,000 × *g* for 1 min in order to elute the RNA. Hep3B cells were grown to 70% confluency in a six-well plate at 37°C and 5% CO_2 in DMEM with 10% FBS and 1% Penicillin/Streptomycin.

RNA sequencing

RNA sequencing was performed by Psomagen using the Illumina Truseq stranded mRNA library, a 40 bp sequencing coverage, 40 million total reads, and a read length of 150 bp PE on a NovaSeq6000 S4. All samples passed Psomagen Quality Control checks for both RNA and cDNA. RNAseq quality was validated by checking for a Q30 greater than or equal to 85% through NovaSeq 6000 and NovaSeq X Plus analysis, a Q30 greater than or equal to 80% through HiseqX analysis, and a Q30 greater than or equal to 70% for 2 × 300 bp through MiSeq analysis. Low-quality bases with a Q less than 20 were trimmed. Subsequently, reads with more than 10% low-quality bases were trimmed. Adapter sequences were then trimmed from remaining reads. Ribosomal RNAs and RNAs mapped to incorrect genomes were filtered out of the dataset. Alignment coverage, depth, and pair-end mapping information were generated based on the percentage of mapped reads, percentage of reads mapped onto specific genomic regions defined by GTF or GFF, 3′ and 5′ bias patterns, the properly paired read percentage, and the strandness of the alignment.

Transcriptomics analysis was performed in BasePair, in which one Principal Component covered 90.53% of variants in HEP3B data and in the mid-40 percentile for different genotypes in *Drosophila* data with quadruplicate samples.

RNA sequencing data analysis

RNA sequencing data was analyzed, and Differential Expression data was generated by Basepair. Data was aligned to the appropriate genome using STAR and gene expression levels were quantified using featureCounts. Differential Expression data was generated using DE-Seq2 and pathway enrichment analysis was performed using GSEA.

MitoBlue staining of human cultured cells

Tissue culture cells were plated in DMEM with 10% FBS and 1% Penicillin/Streptomycin on Ibidi 12-well chamber slides at 30,000 cells/well the day before they were to be stained. The cells were kept overnight at 37°C and 5% CO_2. On the day of the experiment, the complete DMEM was removed and a 5 μM MitoBlue solution in DMEM containing no FBS or PenStrep was applied to the cells. The cells were incubated for 30 min at 37°C out of light. The staining solution was aspirated, and the cells were washed with PBS. 4% v/v PFA was applied to the cells, which were then incubated for 30 min at room temperature out of light. The PFA and rubber chambers were then removed and Vectashield was applied as a mounting medium. The cells were imaged with an Olympus FV1000 microscope. Images of Hep3B cells stained with MitoBlue were processed in Fiji ImageJ on a maximum intensity projection. An auto-threshold was applied to the images through Max Entropy. A watershed was applied and segmented mitochondria. Particles were selected for those between 1 and 10 μm in area and between 0.25 and 1.00 in circularity. All images included in Figure 2 were brightened 20% from originals for best reproduction.

LipidTOX red staining of human cultured cells

Tissue culture cells were plated in DMEM with 10% FBS and 1% Penicillin/Streptomycin on Ibidi 12-well chamber slides at 30,000 cells/well the day before they were to be stained. The cells were kept overnight at 37°C and 5% CO_2. On the day of the experiment, the DMEM was removed and 4% v/v PFA solution, a fixative, was applied to the cells for 30 min at room temperature out of light. The PFA was aspirated, and the cells were washed with PBS. LipidTOX Red diluted 1:1000 in buffer was applied to the cells and they were incubated for 30 min at room temperature out of light. The LipidTOX Red solution and rubber chambers were then removed and Vectashield was applied as a mounting medium. The cells were imaged with an Olympus FV1000 microscope. Maximum projection confocal images of HEK293T cells were analyzed for differences in LipidTOX Red signal intensity. A 145×145 pixel box was used as a sample area, approximately ten cells were included in each pixel box. A histogram was collected of each sample area, with 256 bins collected in each histogram. The scale of pixel intensities was set from 0 to 4096. Each sample was analyzed using this method three times, ensuring that the analyzed areas did not overlap. All LipidTOX images included in Figure 2 were brightened equally for better reproduction. The graph in Figure 2 represents average pixel intensities for sampled regions for one experiment with error bars representing SEM. The experiment was conducted in quadruplicate.

Preparation of fluorescently tagged guanidinylated neomycin-C5 conjugate and uptake experiments

Biotinylated guanidinylated neomycin (GNeo-biotin) was synthesized, as previously described,[44] and stored in water at −20°C. After thawing at room temperature, GNeo-biotin was diluted into PBS to 2.5 μM. To this solution, streptavidin-Cy5 (ST-Cy5, Thermo Fisher) was added to achieve a final molar ratio of 1:5 of fluorophore to biotin. To ensure completion of the biotin-streptavidin reaction, the solution was gently mixed and allowed to incubate at room temperature, shielded from light, for 20 min. Following this incubation, the GNeo-ST-Cy5 conjugate was diluted to the desired concentration in DMEM media. A375 wildtype or NDST1−/− knockout cells were plated at 200,000 cells/well in 6-well tissue culture plates and let adhere overnight. The next day, the cells were washed with PBS and incubated with fluorescent-tagged GNeo-biotin (10 nM) for 1 h at 37°C under an atmosphere of 5% CO2. Control cells were treated with ST-Cy5 only. After incubation, cells were washed twice with PBS, released with 0.05% trypsin/EDTA (Corning), and analyzed by flow cytometry.

MitoTracker red and LipidTOX green uptake studies and flow cytometry

A375 wildtype or NDST1−/− knockout cells were plated at 200,000 cells/well in 6-well tissue culture plates and let adhere overnight. For drug treatments, DMSO or rapamycin (10 μM) was added the next day, then cells were incubated for 24 h at 37°C under an atmosphere of 5% CO2. The next day, the cells were washed with PBS and incubated with MitoTracker Red (1:1000, Thermo) or HCS LipidTOX Green (1:500, Thermo) diluted in DMEM media for 1 h at 37°C under an atmosphere of 5% CO2. After incubation, cells were washed twice with PBS, released with 0.05% trypsin/EDTA (Corning), and analyzed by flow cytometry. Flow cytometry experiments were performed using a CytoFLEX S (Beckman Coulter) flow cytometer (≥10,000 events/sample), and raw data were analyzed using FlowJo Analytical Software v10.8 (Becton Dickinson). Cells were gated according to forward and side scattering. The extent of uptake was quantified using the geometric mean of the fluorescence intensity versus control samples. These values were plotted and further analyzed using GraphPad Prism v10.0.

Seahorse measurement of oxygen consumption rate

The cell's rate of oxidative metabolism of glucose was evaluated with XF Cell Mito-stress Assay in a Seahorse XFe24 analyzer which allows real-time metabolic analysis in live cells. Three cell lines, A375, Hep3B, and HEK293T, were plated on Agilent Seahorse XF24 Cell Culture Microplates (30,000 cells/per well) and were placed in a CO2 incubator overnight. The sensor cartridge used from an Agilent Seahorse XFe24 Extracellular Flux Assay kit was hydrated with Seahorse XF Calibrant (1000 μL/well) overnight in a non-CO2 incubator. Cells were subsequently washed with XF assay media [0.5 mM Glutamine (200 mM solution), 0.5 mM Glucose (1.0 M solution), 0.5 mM Pyruvate (100mM solution), 48.5 mM Seahorse XF DMEM assay medium, pH 7.4]. After washing, cells were incubated in respective media (37°C, 1 h) in a non-CO2

incubator, allowing for temperature/pH equilibration before each measurement in the metabolic analyzer. Each plate contained four wells not seeded with cells to serve as blank controls for temperature-sensitive fluctuations. In the case of HEK293T, there were six control wells, to divide specified wells evenly between three genotypes. The lyophilized drugs from the Seahorse XF Mito Stress kit were diluted in Seahorse XF assay media and loaded into the corresponding injection ports in the sensor cartridge. Following measurements of resting respiration, cells were subsequently treated with Oligomycin (1.5 μM) for the assessment of non-phosphorylating oxygen consumption rate (OCR), with the mitochondrial uncoupler FCCP (1.0 μM) for the evaluation of maximal OCR, and with a combination of Rotenone and Antimycin A (both at 0.5 μM) for estimating extra-mitochondrial OCR. In all cases, three measurements were recorded, each over a 5–8 min interval including mixing and incubating. At the end of the Seahorse run, to allow comparison among different experiments, data were normalized to the total cell amount per well. In all cases, the metabolic parameters of the assay–basal and maximal respiration, proton leak, and ATP production through oxidative phosphorylation– were calculated with Agilent/Seahorse XF Report Generator software and expressed as OCR in pmol/min. The results are illustrated as a representative from at least three independent experiments performed in triplicate or means ± standard error from at least three independent experiments performed in triplicate.

Isolation and culture of primary astrocytes

Primary astrocytes were isolated as described as follows: Fresh mouse brain tissue without cerebellum or brain stem tissue was enzymatically digested then mechanically dissociated with the gentleMACS Dissociater with Heaters. Debris Removal Solution and Red Blood Cell Removal Solution were then used to remove myelin, cell debris, and erythrocytes. Astrocytes were isolated using Anti-ACSA-2 MicroBeads. Microglia were removed by shaking in an incubator overnight and astrocytes were verified as negative for microglia through Iba1 staining. Isolated astrocytes were cultivated in DMEM/F12 with 10% FBS penicillin/streptomycin for two weeks before use.[45]

Astrocyte lipid droplets staining and quantification

Lipid droplets in astrocytes were stained and quantified as follows: HCS LipidTOX Red Neutral Lipid Stain was used to stain astrocytes following the manufacturer's instruction. Isolated astrocytes were cultivated in DMEM/F12 with 10% FBS penicillin/streptomycin for two weeks before use. Medium was removed and cells were washed with PBS 3 times. Cells were then fixed in 4% Paraformaldehyde for 30 min and stained with 1X LipidTOX for 30 min at room temperature. A Zeiss LSM 880 with Airyscan was used to collect Z section images and generate three-dimensional images. The surface module of Imaris 9.3.0 was used to quantify the number and volume of lipid droplets from at least 3 animals or batches of cell cultures; n = 3–8 coverslips/condition; 8 ± 2 cells/coverslip. Each data point represents the averaged value of all cells on a coverslip.[45]

Lenti-Ndst1shRNA transfection

Astrocytes isolated from E18 pregnant C57BL/6J, *APOE3* and *APOE4* knock-in mice were seeded on Poly-D-Lysine coated 12-well or 6-well plate with coverslips at a density of 3×10^5 or 5×10^3 well with complete medium (DMEM/F12 supplemented with 10% Fetal Bovine Serum and 1% Penicillin & Streptomycin), respectively. The lentivirus stocks (Lenti-Ndst1shRNA and scramble) were thawed on ice before transfection. The appropriate volume of virus was diluted into the media (DMEM/F12 supplemented with 10% FBS only) in order to achieve the desired MOI (Multiplicity of infection, 5–10 cells) of virus according to the stock concentration. After 48h incubation, the medium was aspirated, and the cells were washed once with PBS and incubated with complete medium for another 3 days. Astrocytes from 12-well plates were collected for RT-PCR and 6-well plates with coverslip were used for immunostaining. Results were obtained from 4 to 6 independent experiments performed in duplicate wells. Transduction efficiency was assessed by analyzing the number of cells that showed positive for GFP fluorescence after fixation and by staining all cell nuclei with DAPI.

RNA extraction and RT-qPCR from *Drosophila* and human cultured cells

Total RNA was isolated from cultured cells described above using TRIzol and PureLink RNA Mini Kit (Cat# 12183018A, Thermo Fisher). Extracted RNAs were reverse transcribed to cDNA using the SuperScript IV VILO Master (Cat# 11756050, Thermo Fisher). Relative mRNA levels of target genes (Ndst1, Plin2, Gfap, Fasn, Acc, Pparg, Cpt1α, Pgc1α) were amplified by SYBR Green real-time PCR assays in QuantStudio 6 System. The sequence for the Ndst1f primer is CCACAACTATCACAAAGGCATCG. The sequence for the Ndst1R primer is GAAAGGTGTACTTTAGGGCCAC. The sequence for the Plin2F primer is GACCTTGTGTCCTCCGCTTAT. The sequence for the Plin2R primer is CAACCGCAATTTGTGGCTC. The sequence for the HprtF primer is AGTGTTGGATACAGGCCAGAC. The sequence for the HprtR primer is CGTGATTCAAATCCCTGAAGT. The sequence for the GapdhF primer is TGACCTCAACTACATGGTCTACA. The sequence for the GapdhR primer is CTTCCCATTCTCGGCCTTG. The relative gene expression level was calculated by the comparative Ct (ΔΔCt) method when compared to the internal control genes (Hprt, Gapdh, β-actin, RPL13) for individual samples. Results were obtained from 4 independent experiments performed in duplicate wells.

LipidTOX staining

Lipid droplet staining was performed according to the product manual (HCS LipidTOX Neutral Lipid Stains, Cat# H34476 HCS LipidTOX Red neutral lipid stain). Briefly, the incubation medium was aspirated, and enough formaldehyde fixative solution was added to a 6-well plate to cover cells for 30 min at room temperature. Then the fixed cells were rinsed with PBS 3 times and incubated with LipidTOX neutral lipid stain

(1:200 dilution) at room temperature for 30 min. The cells were covered with mounting medium containing DAPI (Cat#H-2000, Vector Laboratories, Inc). Images were then captured with Zeiss Laser-Scanning Microscopy (LSM) 880 with Airyscan detector. z stack images were captured to generate three-dimensional volumetric data. The number and volume of intracellular lipid droplets were quantified using the surface module of Imaris 9.8.0.

QUANTIFICATION AND STATISTICAL ANALYSIS

Avizo image processing

Three-dimensional reconstructions of mitochondria were generated using Avizo software. Outlines of mitochondria were traced through all slices where the structure was visible and interpolated between slices using the built-in Avizo function set to the appropriate slice depth of 100 μm. Images were taken of each mitochondrial reconstruction at an approximately equal zoom for analysis. Quantitative data was obtained using the built-in measurement function of Avizo and analyzed.

Drosophila gene set analysis

FlyEnrichr was used to assess gene set representation for the top 500 significant differentially expressed genes in sfl^{RNAi} of fat body cells[109,110] compared to controls (w^{RNAi}).

Flow Cytometry statistics were analyzed using GraphPad Prism v10.0 (https://www.graphpad.com/) and other statistics were analyzed using Minitab (https://www.minitab.com/en-us/). Details of statistical tests, sample sizes, n, what n represents, and levels of significance can be found in figures and their corresponding figure legends.

Details of statistical tests

ANOVA Tukey Tests and Kolmogorov-Smirnov Tests were used in MiniTab. Two-tailed heteroscedastic T-Tests were performed in Excel. ANOVA Tukey Tests and T-tests were used to analyze collections of data points from multiple experiments. Kolmogorov-Smirnov Tests were used to analyze averaged distributions of pixel intensity from an experiment, with data presented as a representative graph. Data are expressed as mean ± SEM. *p* values of *<0.05, **<0.01, and ***<0.001 were considered as significant.